
Inflationary Flows: Calibrated Bayesian Inference with Diffusion-Based Models

Daniela de Albuquerque

Department of Electrical &
Computer Engineering
School of Medicine
Duke University
Durham, NC 27708

daniela.de.albuquerque@duke.edu

John Pearson

Department of Neurobiology
Department of Electrical &
Computer Engineering
Center for Cognitive Neuroscience
Duke University
Durham, NC 27708

john.pearson@duke.edu

Abstract

Beyond estimating parameters of interest from data, one of the key goals of statistical inference is to properly quantify uncertainty in these estimates. In Bayesian inference, this uncertainty is provided by the posterior distribution, the computation of which typically involves an intractable high-dimensional integral. Among available approximation methods, sampling-based approaches come with strong theoretical guarantees but scale poorly to large problems, while variational approaches scale well but offer few theoretical guarantees. In particular, variational methods are known to produce overconfident estimates of posterior uncertainty and are typically non-identifiable, with many latent variable configurations generating equivalent predictions. Here, we address these challenges by showing how diffusion-based models (DBMs), which have recently produced state-of-the-art performance in generative modeling tasks, can be repurposed for performing calibrated, identifiable Bayesian inference. By exploiting a previously established connection between the stochastic and probability flow ordinary differential equations (pfODEs) underlying DBMs, we derive a class of models, *inflationary flows*, that uniquely and deterministically map high-dimensional data to a lower-dimensional Gaussian distribution via ODE integration. This map is both invertible and neighborhood-preserving, with controllable numerical error, with the result that uncertainties in the data are correctly propagated to the latent space. We demonstrate how such maps can be learned via standard DBM training using a novel noise schedule and are effective at both preserving and reducing intrinsic data dimensionality. The result is a class of highly expressive generative models, uniquely defined on a low-dimensional latent space, that afford principled Bayesian inference.

1 Introduction

In many fields of science, the aim of statistical inference is not only to estimate model parameters of interest from data but to quantify the *uncertainty* in these estimates. In Bayesian inference, for data \mathbf{x} generated from latent parameters \mathbf{z} via a model $p(\mathbf{x}|\mathbf{z})$, this information is encapsulated in the posterior distribution $p(\mathbf{z}|\mathbf{x})$, computation of which requires evaluation of the often intractable normalizing integral $p(\mathbf{x}) = \int p(\mathbf{x}, \mathbf{z}) d\mathbf{z}$. Where accurate uncertainty estimation is required, the gold standard remains sampling-based Markov Chain Monte Carlo (MCMC) methods, which are guaranteed (asymptotically) to produce exact samples from the posterior distribution [1]. However, MCMC methods can be computationally costly and do not readily scale either to large or high-dimensional data sets.

Alternatively, methods based on variational inference (VI) attempt to approximate posterior distributions by optimization, minimizing some measure of divergence between the true posterior and a parameterized set of distributions $q_\phi(\mathbf{z}|\mathbf{x})$ [2]. For example, methods like the variational autoencoder (VAE) [3, 4] minimize the Kullback-Leibler (KL) divergence between true and approximate posteriors, producing bidirectional mappings between data and latent spaces. However, despite their many successes, these models tend to produce blurry data reconstructions and non-unique latent spaces without additional assumptions [5–7]. Similarly, posterior uncertainty estimates are overconfident due to minimization of the reverse (mode-seeking) KL divergence [8, 9]. By contrast, normalizing flow (NF) models [10, 11] work by applying a series of bijective transformations to a simple base distribution (usually uniform or Gaussian) to deterministically convert samples to a desired target distribution. While NFs have been successfully used for posterior approximation [12–16] and produce higher-quality samples, the requirement that the Jacobian of each transformation be simple to compute often requires a high number of transformations, and these transformations do not alter the the dimensionality of their inputs, resulting in latent spaces with thousands of dimensions. Thus, these models lack a key advantage of VAEs and their ilk: a compressed representation of the data.

More recently, diffusion-based models (DBMs) [17–24] have been shown to achieve state-of-the-art results in several generative tasks, including image, sound, and text-to-image generation. These models work by stipulating a fixed forward noising process (i.e., forward SDE), wherein Gaussian noise is incrementally added to samples of the target data distribution until all information in the original data is degraded. To generate samples from the target distribution, one then needs to simulate the reverse de-noising process (reverse SDE [25]) which requires knowledge of the score of the intermediate “noised” transitional densities. Estimation of this score function across multiple noise levels is the key component of DBM model training, typically using a de-noising score matching objective [26, 19, 21]. Yet, despite their excellent performance as *generative* models, DBMs, unlike VAEs or NFs, do not readily lend themselves to *inference*. In particular, because DBMs use a *diffusion* process to transform the data distribution, they fail to preserve local structure in the data (**Figure 1**), and uncertainty under this mapping is high at its endpoint because of continuous noise injection and resultant mixing. Moreover, because the final distribution—Gaussian white noise of the same dimension—must have *higher* entropy than the original data, there is no data compression.

Thus, despite tremendous improvements in sample quality, modern generative models do not lend themselves to one of the key modeling goals in scientific applications: accurate Bayesian inference. Here, we address this challenge by demonstrating how a novel DBM variant that we call *inflationary flows* can, in fact, produce calibrated, identifiable Bayesian inference. **Specifically, our contributions are:** **First**, we show how a previously established link between the SDE defining diffusion models and the probability flow ODE (pfODE) that gives rise to the same Fokker-Planck equation [21] can be used to define a *unique, deterministic* map between the original data and an asymptotically Gaussian distribution. This map is bidirectional, preserves local neighborhoods, and has controllable numerical error, making it suitable for rigorous uncertainty quantification. **Second**, we define two classes of flows that correspond to novel noise injection schedules in the forward SDE of the diffusion model. The first of these preserves a measure of dimensionality, the participation ratio (PR) [27], based on second-order data statistics, preventing an effective *increase* in data dimensionality with added noise, while the second flow *reduces* PR, providing *data compression*. **Finally**, we demonstrate experimentally that inflationary flows indeed preserve local neighborhood structure, allowing for sampling-based uncertainty estimation, and that these models continue to provide high-quality generation under compression, even from latent spaces reduced to as little as 2% of the nominal data dimensionality. As a result, inflationary flows offer excellent generative performance while affording data compression and accurate uncertainty estimation for scientific applications.

2 Three views of diffusion-based models

As with standard DBMs, we assume a data distribution $p_0(\mathbf{x}) = p_{\text{data}}(\mathbf{x})$ at time $t = 0$, transformed via a forward noising process defined by the stochastic differential equation [e.g., 17, 19]:

$$d\mathbf{x} = \mathbf{f}(\mathbf{x}, t)dt + \mathbf{G}(\mathbf{x}, t) \cdot d\mathbf{W}, \quad (1)$$

with most DBMs assuming linear drift ($\mathbf{f} = f(t)\mathbf{x}$) and isotropic noise ($\mathbf{G} = \sigma(t)\mathbb{1}$) that monotonically increases over time [28]. As a result, for $\int_0^T \sigma(T)dt \gg \sigma_{\text{data}}$, $p_T(\mathbf{x})$ becomes essentially indistinguishable from an isotropic Gaussian (**Figure 1, left**). DBMs work by learning an approxima-

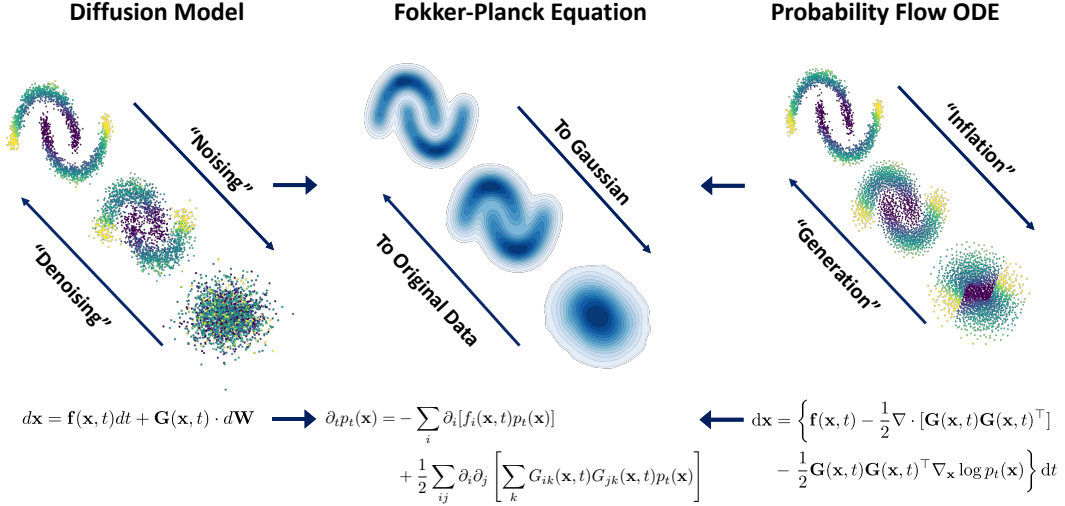


Figure 1: **SDE-ODE Duality of diffusion-based models.** The forward (noising) SDE defining the DBM (left) gives rise to a sequence of marginal probability densities whose temporal evolution is described by a Fokker-Planck equation (FPE, middle). But this correspondence is not unique: the probability flow ODE (pfODE, right) gives rise to the *same* FPE. That is, while both the SDE and the pfODE transform the data distribution in the same way, the former is noisy and mixing while the latter is deterministic and neighborhood-preserving. Both models require knowledge of the score function $\nabla_x \log p_t(\mathbf{x})$, which can be learned by training either.

tion to the reverse SDE [25, 19–21, 29],

$$d\mathbf{x} = \left\{ \mathbf{f}(\mathbf{x}, t) - \nabla \cdot [\mathbf{G}(\mathbf{x}, t) \mathbf{G}(\mathbf{x}, t)^\top] - \mathbf{G}(\mathbf{x}, t) \mathbf{G}(\mathbf{x}, t)^\top \nabla_x \log p_t(\mathbf{x}) \right\} dt + \mathbf{G}(\mathbf{x}, t) \cdot d\bar{\mathbf{W}}, \quad (2)$$

where $\bar{\mathbf{W}}$ is time-reversed Brownian motion. In practice, this requires approximating the score function $\nabla_x \log p_t(\mathbf{x})$ by incrementally adding noise according to the schedule $\sigma(t)$ of the forward process and then requiring that denoising by (2) match the original sample. The fully trained model then generates samples from the target distribution by starting with $\mathbf{x}_T \sim \mathcal{N}(\mathbf{0}, \sigma^2(T) \mathbb{1})$ and integrating (2) in reversed time.

As previously shown, this diffusive process gives rise to a series of marginal distributions $p_t(\mathbf{x})$ satisfying a Fokker-Planck equation (Figure 1, middle) [21, 28],

$$\partial_t p_t(\mathbf{x}) = - \sum_i \partial_i [f_i(\mathbf{x}, t) p_t(\mathbf{x})] + \frac{1}{2} \sum_{ij} \partial_i \partial_j \left[\sum_k G_{ik}(\mathbf{x}, t) G_{jk}(\mathbf{x}, t) p_t(\mathbf{x}) \right], \quad (3)$$

where $\partial_i \equiv \frac{\partial}{\partial x_i}$. In the “variance preserving” noise schedule of [21], (3) has as its stationary solution an isotropic Gaussian distribution. This “distributional” perspective views the forward process as a means of transforming the data into an easy-to-sample form (as with normalizing flows) and the reverse process as a means of data generation.

However, in addition to the SDE and FPE perspectives, Song et al. [21] also showed that (3) is satisfied by the marginals of a different process with no noise term, the so-called *probability flow ODE* (pfODE):

$$d\mathbf{x} = \left\{ \mathbf{f}(\mathbf{x}, t) - \frac{1}{2} \nabla \cdot [\mathbf{G}(\mathbf{x}, t) \mathbf{G}(\mathbf{x}, t)^\top] - \frac{1}{2} \mathbf{G}(\mathbf{x}, t) \mathbf{G}(\mathbf{x}, t)^\top \nabla_x \log p_t(\mathbf{x}) \right\} dt. \quad (4)$$

Unlike (1), this process is deterministic, and data points evolve smoothly (Figure 1, right), resulting in a flow that preserves local neighborhoods. Moreover, the pfODE is uniquely defined by $\mathbf{f}(\mathbf{x}, t)$, $\mathbf{G}(\mathbf{x}, t)$, and the score function. This connection between the marginals satisfying the SDEs of diffusion processes and *deterministic flows* described by an equivalent ODE has also been recently explored in the context of flow matching models [30–35], a connection on which we elaborate in Section 7.

In the following sections, we show how this pfODE, constructed using a score function estimated by training the corresponding DBM, can be used to map points from $p_{\text{data}}(\mathbf{x})$ to a compressed latent space in a manner that affords accurate uncertainty quantification.

3 Inflationary flows

As argued above, the probability flow ODE offers a means of deterministically transforming an arbitrary data distribution into a simpler form via a score function learnable through DBM training. Here, we introduce a specialized class of pfODEs, inflationary flows, that follow from an intuitive picture of local dynamics and asymptotically give rise to stationary Gaussian solutions of (3).

We begin by considering a sequence of marginal transformations in which points in the original data distribution are convolved with Gaussians of increasingly larger covariance $\mathbf{C}(t)$:

$$p_t(\mathbf{x}) = p_0(\mathbf{x}) * \mathcal{N}(\mathbf{x}; \mathbf{0}, \mathbf{C}(t)). \quad (5)$$

It is straightforward to show (Appendix A.1) that this class of time-varying densities satisfies (3) when $\mathbf{f} = \mathbf{0}$ and $\mathbf{G}\mathbf{G}^\top = \dot{\mathbf{C}}$. This can be viewed as a process of deterministically “inflating” each point in the data set, or equivalently as smoothing the underlying data distribution on ever coarser scales, similar to denoising approaches to DBMs [36, 37]. Eventually, if the smoothing kernel grows much larger than Σ_0 , the covariance in the original data, total covariance $\Sigma(t) \equiv \Sigma_0 + \mathbf{C}(t) \rightarrow \mathbf{C}(t)$, $p_t(\mathbf{x}) \approx \mathcal{N}(\mathbf{0}, \mathbf{C}(t))$, and all information has been removed from the original distribution. However, because it is numerically inconvenient for the variance of the asymptotic distribution $p_\infty(\mathbf{x})$ to grow much larger than that of the data, we follow previous work in adding a time-dependent coordinate rescaling $\tilde{\mathbf{x}}(t) = \mathbf{A}(t) \cdot \mathbf{x}(t)$ [21, 28], resulting in an asymptotic solution $p_\infty(\mathbf{x}) = \mathcal{N}(\mathbf{0}, \mathbf{A}\Sigma\mathbf{A}^\top)$ of the corresponding Fokker-Planck equation when $\dot{\Sigma} = \dot{\mathbf{C}}$ and $\dot{\mathbf{A}}\Sigma\mathbf{A}^\top + \mathbf{A}\Sigma\dot{\mathbf{A}}^\top = \mathbf{0}$ (Appendix A.2). Together, these assumptions give rise to the pfODE (Appendix A.3):

$$\frac{d\tilde{\mathbf{x}}}{dt} = \mathbf{A}(t) \cdot \left(-\frac{1}{2} \dot{\mathbf{C}}(t) \cdot \nabla_{\mathbf{x}} \log p_t(\mathbf{x}) \right) + \left(\dot{\mathbf{A}}(t) \cdot \mathbf{A}^{-1}(t) \right) \cdot \tilde{\mathbf{x}}, \quad (6)$$

where the score function is evaluated at $\mathbf{x} = \mathbf{A}^{-1} \cdot \tilde{\mathbf{x}}$. Notably, (6) is equivalent to the general pfODE form given in [28] in the case both $\mathbf{C}(t)$ and $\mathbf{A}(t)$ are isotropic (Appendix A.4), with $\mathbf{C}(t)$ playing the role of injected noise and $\mathbf{A}(t)$ the role of the scale schedule. In the following sections, we will show how to choose both of these in ways that either preserve or reduce intrinsic data dimensionality.

3.1 Dimension-preserving flows

In standard DBMs, the final form of the distribution $p_T(\mathbf{x})$ approximates an isotropic Gaussian distribution, typically with unit variance. As a result, these models *increase* the effective dimensionality of the data, which may begin as a low-dimensional manifold embedded within \mathbb{R}^d . Thus, even maintaining intrinsic data dimensionality requires both a definition of dimensionality and a choice of flow that preserves this dimension. In this work, we consider a particularly simple measure of dimensionality, the participation ratio (PR), first introduced by Gao et al. [27]:

$$\text{PR}(\Sigma) = \frac{\text{tr}(\Sigma)^2}{\text{tr}(\Sigma^2)} = \frac{(\sum_i \sigma_i^2)^2}{\sum_i \sigma_i^4} \quad (7)$$

where Σ is the covariance of the data with eigenvalues $\{\sigma_i^2\}$. PR is invariant to linear transforms of the data, depends only on second-order statistics, is 1 when Σ is rank-1, and is equal to the nominal dimensionality d when $\Sigma \propto \mathbb{1}_{d \times d}$. In Appendix C.1 we report this value for several benchmark image datasets, confirming that in all cases, PR is substantially lower than the nominal data dimensionality.

To construct flows that preserve this measure of dimension, following (5), we write total variance as $\Sigma(t) = \text{diag}(\sigma^2(t)) = \mathbf{C}(t) + \Sigma_0$, where Σ_0 is the original data covariance and $\mathbf{C}(t)$ is our time-dependent smoothing kernel. Moreover, we will choose $\mathbf{C}(t)$ to be diagonal in the eigenbasis of Σ_0 and work in that basis, in which case $\Sigma(t) = \text{diag}(\sigma^2(t))$ and we have (Appendix A.6):

$$d\text{PR} = 0 \iff \left(\mathbf{1} - \text{PR}(\sigma^2) \frac{\sigma^2}{\sum_k \sigma_k^2} \right) \cdot d\sigma^2 = 0. \quad (8)$$

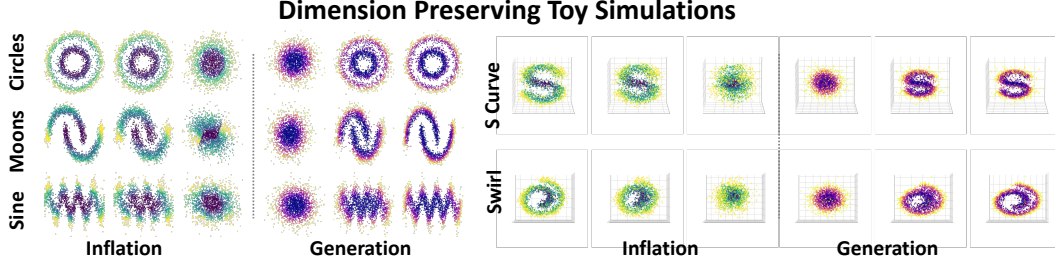


Figure 2: **Dimension-preserving flows for toy datasets.** Numerical simulations of dimension-preserving flows for five sample toy datasets. Left sequences of sub-panels show results for integrating the pfODE forward in time (inflation); right sub-panels show results of integrating the same system backwards in time (generation) (Appendix B.3). Simulations were conducted with score approximations obtained from neural networks trained on each respective toy dataset (Appendix B.4.1).

The simplest solution to this constraint is a proportional inflation, $\frac{d}{dt}(\sigma^2) = \rho\sigma^2$, along with a rescaling along each principal axis:

$$C_{jj}(t) = \sigma_j^2(t) - \sigma_{0j}^2 = \sigma_{0j}^2(e^{\rho t} - 1) \quad A_{jj}(t) = \frac{A_{0j}}{\sigma_j(t)} = \frac{A_{0j}}{\sigma_{0j}}e^{-\rho t/2}. \quad (9)$$

As with other flow models based on physical processes like diffusion [17] or electrostatics [38, 39], our use of the term inflationary flows for these choices is inspired by cosmology, where a similar process of rapid expansion exponentially suppresses local fluctuations in background radiation density [40]. However, as a result of our coordinate rescaling, the effective covariance $\tilde{\Sigma} = \mathbf{A}\Sigma\mathbf{A}^\top = \text{diag}(A_{0j}^2)$ remains constant (so $d\tilde{\sigma}^2 = \mathbf{0}$ trivially), and the additional conditions of Appendix A.2 are satisfied, such that $\mathcal{N}(\mathbf{0}, \tilde{\Sigma})$ is a stationary solution of the relevant rescaled Fokker-Planck equation. As **Figure 2** shows, these choices result in a version of (6) that smoothly maps nonlinear manifolds to Gaussians and can be integrated in reverse to generate samples of the original data.

3.2 Dimension-reducing flows

In the previous section, we saw that isotropic inflation preserves intrinsic data dimensionality as measured by PR. Here, we generalize and consider *anisotropic* inflation at different rates along each of the eigenvectors of Σ : $\frac{d}{dt}(\sigma^2) = \rho\mathbf{g} \odot \sigma^2$ with $g_* \equiv \max(\mathbf{g})$ so that the fastest inflation rate is ρg_* . Then, if we take $g_i = g_*$ for $i \in \{i_1, i_2, \dots, i_K\}$ and $g_i < g_*$ for the other dimensions,

$$\text{PR}(\Sigma(t)) = \frac{(\sum_i \sigma_{0i}^2 e^{(g_i - g_*)\rho t})^2}{\sum_i (\sigma_{0i}^2 e^{(g_i - g_*)\rho t})^2} \xrightarrow{t \rightarrow \infty} \frac{(\sum_{k=1}^K \sigma_{0i_k}^2)^2}{\sum_{j=1}^K \sigma_{0i_j}^4} \quad (10)$$

which is the dimension that would be achieved by simply truncating the original covariance matrix in a manner set by our choice of \mathbf{g} . Here, unlike in (9), we do not aim for rescaling to compensate for expansion along each dimension, since that would undo the effect of differential inflation rates. Instead, we choose a single global rescaling factor $\alpha(t) \propto A_0 \exp(-\rho g_* t/2)$, which converges to a Gaussian distribution with covariance matching that of the initial data in all dimensions with $g_i = g_*$.

Two additional features of this class of flows are worth noting: First, the final scale ratio of preserved to shrunken dimensions for finite integration times T is governed by the quantity $e^{\rho(g_* - g_i)T}$ in (10). For good compression, we want this number to be very large, but as we show in Appendix A.4, this corresponds to a maximum injected noise of order $e^{\rho(g_* - g_i)T/2}$ in the equivalent DBM. That is, the compression one can achieve with inflationary flows is constrained by the range of noise levels over which the score function can be accurately estimated, and this is quite limited in typical models. Second, despite the appearance given by (10), the corresponding flow *is not* simply a linear projection to the top K principal components: though higher PCs are selectively removed by dimension-reducing flows via exponential shrinkage, individual particles are repelled by *local* density as captured by the score function (6), and this term couples different dimensions even when \mathbf{C} and \mathbf{A}

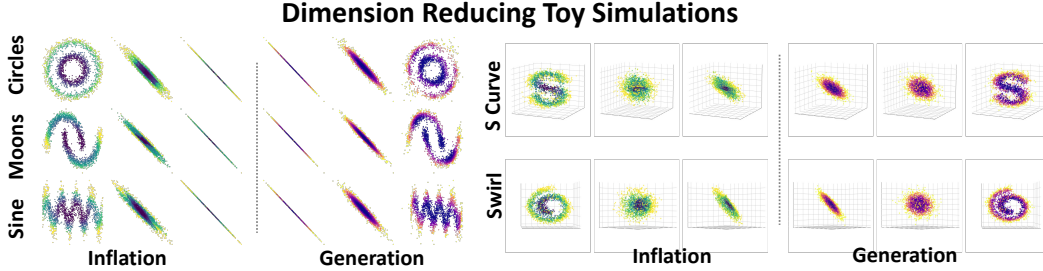


Figure 3: **Dimension-reducing flows for toy datasets.** Numerical simulations of dimension-reducing flows for the same five datasets as in **Figure 2**. For 2D datasets, we showcase reduction from two to one dimension, while 3D datasets are reduced to two dimensions. Colors and layouts are the same as in **Figure 2**, with scores again estimated using neural networks trained on each example. Additional results showcasing (1) similar flows further compressing two-dimensional manifolds embedded in $D = 3$ space, and (2) effects of adopting different scaling schemes for target data are given in Appendices C.2.1 and C.2.2, respectively.

are diagonal. Thus, the final positions of particles in the retained dimensions depend on their initial positions in the full space, producing a nonlinear map (**Figure 3**).

4 Score function approximation from DBMs

Having chosen inflation and rescaling schedules, the last component needed for the pfODE (6) is the score function $s(\mathbf{x}, t) \equiv \nabla_{\mathbf{x}} \log p_t(\mathbf{x})$. Our strategy will be to exploit the correspondence described above between diffusion models (1) and pfODEs (4) that give rise to the same marginals (3). That is, we will learn an approximation to $s(\mathbf{x}, t)$ by fitting the DBM corresponding to our desired pfODE, since both make use of the same score function.

Briefly, in line with previous work on DBMs [28], we train neural networks to estimate a de-noised version $\mathbf{D}(\mathbf{x}, \mathbf{C}(t))$ of a noise-corrupted data sample \mathbf{x} given noise level $\mathbf{C}(t)$ (cf. Appendix A.4 for the correspondence between $\mathbf{C}(t)$ and noise). That is, we model $\mathbf{D}_\theta(\mathbf{x}, \mathbf{C}(t))$ using a neural network and train it by minimizing a standard L_2 de-noising error:

$$\mathbb{E}_{\mathbf{y} \sim \text{data}} \mathbb{E}_{\mathbf{n} \sim \mathcal{N}(\mathbf{0}, \mathbf{C}(t))} \|\mathbf{D}(\mathbf{y} + \mathbf{n}; \mathbf{C}(t)) - \mathbf{y}\|_2^2 \quad (11)$$

De-noised outputs can then be used to compute the desired score term using $\nabla_{\mathbf{x}} \log p(\mathbf{x}, \mathbf{C}(t)) = \mathbf{C}^{-1}(t) \cdot (\mathbf{D}(\mathbf{x}; \mathbf{C}(t)) - \mathbf{x})$ [21, 28]. Moreover, as in [28], we also adopt a series of preconditioning factors aimed at making training with the above L_2 loss and our noising scheme more amenable to gradient descent techniques (Appendix B.1).

5 Calibrated uncertainty estimates from inflationary flows

As with other implicit models, our inflationary flows provide a deterministic link between complex data and simplified distributions with tractable sampling properties. This mapping requires integrating the pfODE (6) for a given choice of $\mathbf{C}(t)$ and $\mathbf{A}(t)$ and an estimate of the score function of the original data. As a result, sampling-based estimates of uncertainty are trivial to compute: given a prior $\pi(\mathbf{x})$ over the data (e.g., a Gaussian ball centered on a particular example \mathbf{x}_0), this can be transformed into an uncertainty on the dimension-reduced space by sampling $\{\mathbf{x}_j\} \sim \pi(\mathbf{x})$ and integrating (6) forward to generate samples from $\int p(\mathbf{x}_T | \mathbf{x}_0) \pi(\mathbf{x}_0) d\mathbf{x}_0$. As with MCMC, these samples can be used to construct either estimates of the posterior or credible intervals. Moreover, because the pfODE is unique given \mathbf{C} , \mathbf{A} , and the score, the model is *identifiable* when conditioned on these choices.

The only potential source of error, apart from Monte Carlo error, in the above procedure arises from the fact that the score function used in (6) is only an *estimate* of the true score. While it is possible that integrating noisy estimates of the score could produce errant sample mappings, results shown in **Figures 4B–C** suggest that such numerical errors do not seem to accumulate in cases where they can be compared with exact results. This is because, empirically, score estimates do not appear to be

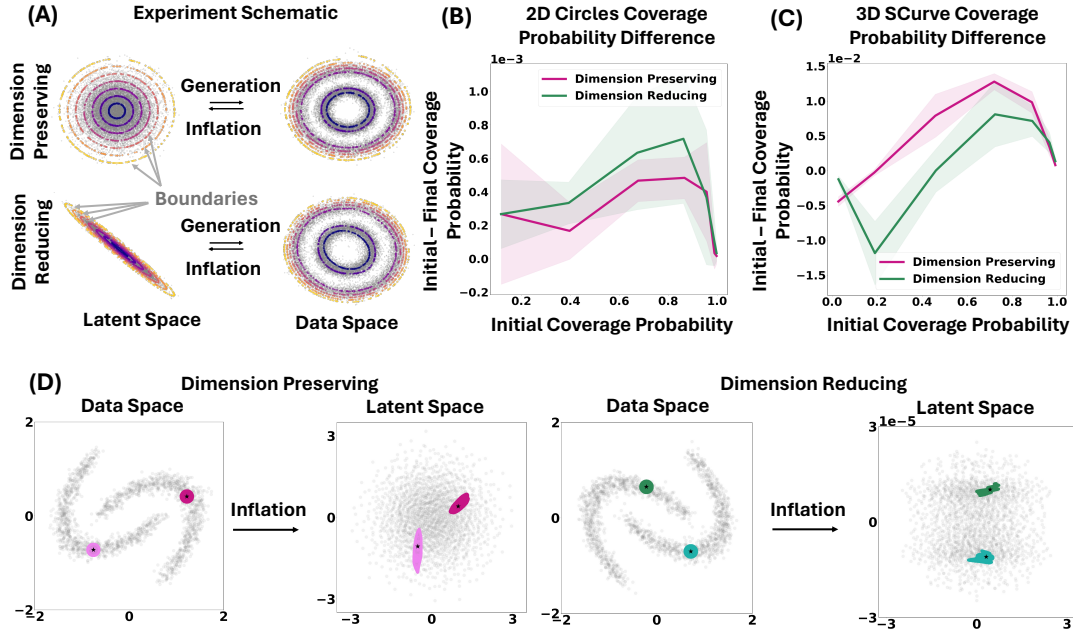


Figure 4: **Calibration experiments.** For select toy datasets, we numerically assessed coverage during the inflation and generation procedures (Appendix B.6). (A) We constructed fixed coverage sets by sampling data points at fixed Mahalanobis radii from the centers of each distribution and creating alpha shapes (2D) or meshes (3D). (B–C) We then quantified the change in coverage fraction for each of these sets at the end of either process. Lines represent means and shaded regions ± 2 standard deviations across three sets of random seeds. (D) Illustration of the effect of flows on set geometry. While both types of flows distort the shapes of initial sets, they do preserve local neighborhoods, even when one dimension is compressed by five orders of magnitude.

Table 1: FID and Round-Trip MSE Mean $\pm 2\sigma$ for benchmark datasets

Metric	Dataset	PRP	PRR to 2%	PRR to 10%	PRR to 20%
FID	CIFAR-10	17.01 ± 0.10	22.23 ± 0.16	23.63 ± 0.13	25.93 ± 0.40
Round-Trip MSE	CIFAR-10	0.23 ± 0.03	2.06 ± 0.04	2.25 ± 0.01	4.16 ± 0.39
FID	AFHQv2	11.89 ± 0.08	13.07 ± 0.07	13.67 ± 0.09	16.77 ± 0.14
Round-Trip MSE	AFHQv2	0.38 ± 0.04	5.57 ± 0.20	7.95 ± 0.31	8.17 ± 0.08

strongly auto-correlated in time (Appendix C.3), suggesting that $\hat{s}(x, t)$, the score estimate, is well approximated as a scaled colored noise process and the corresponding pfODE as an SDE. In such a case, standard theorems for SDE integration show that while errors due to noise do accumulate, these can be mitigated by a careful choice of integrator and ultimately controlled by reducing step size [41, 42]. Below, we verify this empirically in both low-dimensional examples and with round-trip integration of the pfODE in high-dimensional datasets.

6 Experiments

To verify that inflationary flows successfully compress high-dimensional data, we compressed two benchmark datasets (CIFAR-10 [43], AFHQv2 [44]) to 20%, 10%, and 2% of their nominal dimensionality and examined their round-trip and pure generative performance. For estimating score, we used DBM networks trained using the scheme of [28] combined with the novel scaling, noise, and preconditioning proposed above (see Appendices B.1, B.4.2 for details; code available at [45]).

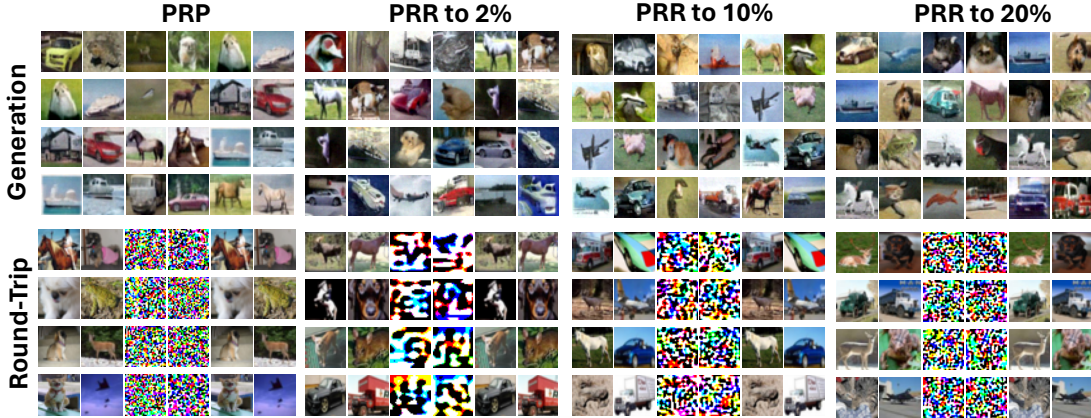


Figure 5: **Generation and Round-Trip Experiments for CIFAR-10.** **Top row:** Generated samples for each flow schedule (PR-Preserving (PRP), and PR-Reducing to 2%, 10%, and 20%). **Bottom row:** Results for round-trip experiments. Leftmost columns are original samples, middle columns are samples mapped to Gaussian latent spaces, and rightmost columns are recovered samples.

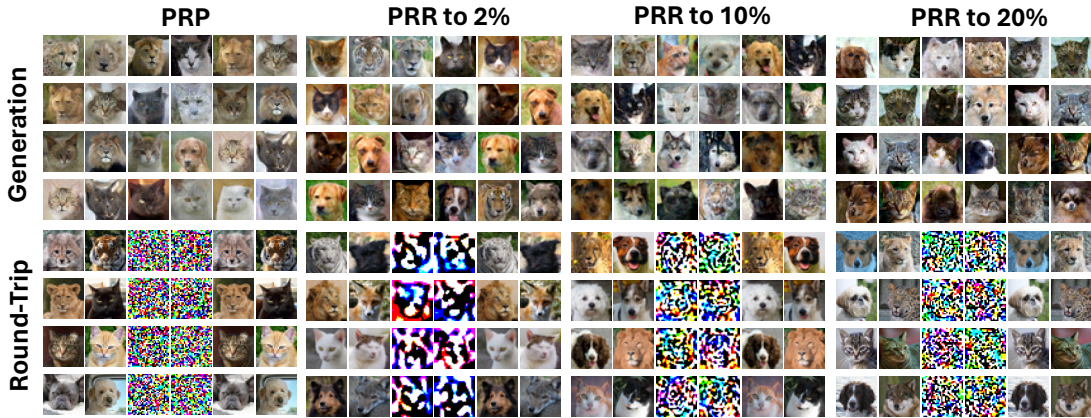


Figure 6: **Generation and Round-Trip Experiments for AFHQv2.** Layout and setup same as for Figure 5 - see Appendices B.5.2, B.5.1 for details.

In **Figures 5** and **6**, we show 24 randomly generated target distribution samples for each schedule (PR-Preserving (PRP), PR-Reducing to 20%, 10%, and 2% (PRR to 20%, 10%, 2%)) and benchmark image dataset (CIFAR-10, AFHQv2). In addition, we show computed Frechet Inception Distance (FID) scores [46] over three different sets of 50,000 randomly generated images for each of these schedules and for both datasets (**Table 1**). Note that preserving intrinsic dimension (PRP schedules) leads to better (smaller) FID scores, as expected. Perhaps surprisingly, increasing the number of preserved dimensions in the PR-Reducing regimes leads to *worse* (i.e., higher) FID scores. This is because retaining more dimensions in our PR-Reducing schedules leads to larger scale gaps between our preserved and compressed dimensions (i.e., larger $e^{\rho(g_* - g_i)T}$), thus increasing the required noise range over which networks must optimally estimate scores. That is, PR-Reducing schedules with higher numbers of preserved-dimensions pose a more challenging learning problem (Appendix B.2).

Additionally, **Figures 5** and **6** also show results for round-trip integration (from data to compressed space and back) for eight random samples across the same experimental configurations and datasets. Reconstructions are qualitatively good across all conditions. Of note, these networks produce inflated representations that resemble true low-rank Gaussian samples, consistent with a reduced-dimensional latent space (see PR-Reducing to 2%, middle columns). In **Table 1**, we also include mean squared errors (MSEs) for each such round-trip experiment (across all schedules and datasets), computed over

3 randomly sampled sets, each with 10K images. Trends observed here are similar to the ones seen for FID experiments. PR-Preserving networks produced lower MSEs overall, whereas PR-Reducing networks with higher percentage of preserved dimensions (i.e., 20%) yielded higher MSEs than PR-Reducing networks with smaller number of preserved dimensions (i.e., 2%). Together, these results suggest that dimension reduction with inflationary flows may necessitate trade-offs between effective compression and the difficulty of score estimation, as noted above.

7 Discussion

Here, we have proposed a new type of implicit probabilistic model based on the probability flow ODE (pfODE) in which it is possible to perform calibrated, identifiable Bayesian inference on a reduced-dimension latent space via sampling and integration. To do so, we have leveraged a correspondence between pfODEs and diffusion-based models by means of their associated Fokker-Planck equations, and we have demonstrated that such models continue to produce high-quality generated samples even when latent spaces are as little as 2% of the nominal data dimension. More importantly, the uniqueness and controllable error of the generative process make these models an attractive approach in cases where accurate uncertainty estimates are required.

Limitations: One limitation of our model is its reliance on the participation ratio (7) as a measure of dimensionality. Because PR relies only on second-order statistics and our proposals (9) are formulated in the data eigenbasis, our method tends to favor the top principal components of the data when reducing dimension. However, as noted above, this is not simply via truncation of lower PCs, since dimensions still mix via coupling to the score function in (6). Nonetheless, solutions to the condition (8) that preserve (or reduce) more complex dimensionality measures might lead to even stronger compressions for curved manifolds (Appendix C.2.1), and more sophisticated choices for noise and rescaling schedules in (6) might lead to compressions that do not simply remove information along fixed axes, more similar to [47]. That is, we believe much more interesting classes of flows are possible. A second limitation is that mentioned in Section and our experiments: our schedule requires training DBMs over much larger ranges of noise than are typically used, and this results in noticeable tradeoffs in compression performance as the number of dimensions is varied.

Related work: This work draws on several related lines of research, including work on using DBMs as likelihood estimation machines [29, 48, 22], relations with normalizing flows and hierarchical VAEs [48, 24, 49], and generative flow networks [50]. By contrast, our focus is on the use of DBMs to learn score functions estimates for implicit probabilistic models, with the ultimate goal of performing accurate inference. In this way, it is also closely related to work on denoising models [36, 37, 47, 51] that cast that process in terms of statistical inference and to models that use DBMs for de-blurring and in-painting [52, 53]. However, this work is distinct from several models that use reversal of deterministic transforms to train generative models [54–57]. Whereas those models work by removing information from each sample \mathbf{x} , our proposal relies critically on adjusting the local density of samples with respect to one another, moving the marginal distribution toward a Gaussian.

Our work is also similar to methods that use DBMs to construct samplers for unnormalized distributions [58–62]. Whereas we begin with samples from the target distribution and aim to learn latent representations, those studies start with a pre-specified form for the target distribution and aim to generate samples. Other groups have also leveraged sequential Monte Carlo (SMC) techniques to construct new types of denoising diffusion samplers for, e.g., conditional generation [63–65]. While our goals are distinct, we believe that the highly simplified Gaussian distribution of our latent spaces may potentially render joint and conditional generation more tractable in future models. Finally, while many prior studies have considered compressed representations for diffusion models [66–69], typically in an encoder-decoder framework, the focus there has been on generative quality, not inference. Along these lines, the most closely related to our work here is [70], which considered diffusion along linear subspaces as a means of improving sample quality in DBMs, though there again, the focus was on improving generation and computational efficiency, not statistical inference.

Yet another line of work closely related to ours is the emerging literature on *flow matching* [30–33] models, which utilize a simple, time-differentiable, “interpolant” function to specify *conditional* families of distributions that continuously map between specified initial and final densities. That is, the interpolant functions define flows that map samples from a base distribution $\rho_0(\mathbf{x})$ to samples from a target distribution $\rho_1(\mathbf{x})$. Typically, these approaches rely on a simple quadratic objective that

attempts to match the *conditional* flow field, which can be computed in closed form without needing to integrate the corresponding ODE. As shown in Appendix A.5, the pfODEs obtained using our proposed scaling and noising schedules are *equivalent* to the ODEs obtained by using the “Gaussian paths formulation” from [30] when the latter are generalized to full covariance matrices. As a result, our models are amenable to training using flow-matching techniques, suggesting that faster training and inference schemes may be possible through leveraging connections between flow matching and optimal transport [34, 35, 71, 32]

Broader impacts: Works like this one that focus on improving generative models risk contributing to an increasingly dangerous set of tools capable of creating misleading, exploitative, or plagiarized content. While this work does not seek to improve the quality of data generation, it does propose a set of models that feature more informative latent representations of data, which could potentially be leveraged to those ends. However, this latent data organization may also help to mitigate certain types of content generation by selectively removing, prohibiting, or flagging regions of the compressed space corresponding to harmful or dangerous content. We believe this is a promising line of research that, if developed further, might help address privacy and security concerns raised by generative models.

References

- [1] Christian P. Robert and George Casella. *Monte Carlo Statistical Methods*. Springer Texts in Statistics. Springer New York, New York, NY, 2004. ISBN 978-1-4419-1939-7. doi: 10.1007/978-1-4757-4145-2. URL <http://link.springer.com/10.1007/978-1-4757-4145-2>.
- [2] David M. Blei, Alp Kucukelbir, and Jon D. McAuliffe. Variational inference: A review for statisticians. *Journal of the American Statistical Association*, 112(518):859–877, April 2017. ISSN 0162-1459, 1537-274X. doi: 10.1080/01621459.2017.1285773. arXiv: 1601.00670.
- [3] Diederik P. Kingma and Max Welling. Auto-encoding variational bayes. *arXiv:1312.6114 [cs, stat]*, May 2014. URL <http://arxiv.org/abs/1312.6114>. arXiv: 1312.6114.
- [4] Danilo Jimenez Rezende, Shakir Mohamed, and Daan Wierstra. Stochastic backpropagation and approximate inference in deep generative models. In *International conference on machine learning*, pages 1278–1286. PMLR, 2014.
- [5] Ilyes Khemakhem, Diederik Kingma, Ricardo Monti, and Aapo Hyvarinen. Variational autoencoders and nonlinear ica: A unifying framework. In *International Conference on Artificial Intelligence and Statistics*, pages 2207–2217. PMLR, 2020.
- [6] Miles Martinez and John Pearson. Reproducible, incremental representation learning with Rosetta VAE. In *NeurIPS Bayesian Deep Learning Workshop*, 2021. URL <http://bayesiandeeplearning.org>.
- [7] Luca Moschella, Valentino Maiorca, Marco Fumero, Antonio Norelli, Francesco Locatello, and Emanuele Rodolà. Relative representations enable zero-shot latent space communication. In *The Eleventh International Conference on Learning Representations*, 2023. URL <https://openreview.net/forum?id=Src-nwieGJ>.
- [8] Christopher Bishop. *Pattern Recognition and Machine Learning*. Springer, New York, 2006.
- [9] Ryan Giordano, Tamara Broderick, and Michael I Jordan. Covariances, robustness, and variational bayes. *Journal of machine learning research*, 19(51):1–49, 2018.
- [10] George Papamakarios, Eric Nalisnick, Danilo Jimenez Rezende, Shakir Mohamed, and Balaji Lakshminarayanan. Normalizing flows for probabilistic modeling and inference. *Journal of Machine Learning Research*, 22(57):1–64, 2021.
- [11] Ivan Kobyzev, Simon JD Prince, and Marcus A Brubaker. Normalizing flows: An introduction and review of current methods. *IEEE transactions on pattern analysis and machine intelligence*, 43(11):3964–3979, 2020.
- [12] Danilo Rezende and Shakir Mohamed. Variational inference with normalizing flows. In Francis Bach and David Blei, editors, *Proceedings of the 32nd International Conference on Machine Learning*, volume 37 of *Proceedings of Machine Learning Research*, pages 1530–1538, Lille, France, 07–09 Jul 2015. PMLR. URL <https://proceedings.mlr.press/v37/rezende15.html>.
- [13] Durk P Kingma, Tim Salimans, Rafal Jozefowicz, Xi Chen, Ilya Sutskever, and Max Welling. Improved variational inference with inverse autoregressive flow. *Advances in neural information processing systems*, 29, 2016.
- [14] Rianne van den Berg, Leonard Hasenclever, Jakub M. Tomczak, and Max Welling. Sylvester normalizing flows for variational inference. (arXiv:1803.05649), February 2019. URL <http://arxiv.org/abs/1803.05649>. arXiv:1803.05649 [cs, stat].
- [15] Christos Louizos and Max Welling. Multiplicative normalizing flows for variational bayesian neural networks. In *International Conference on Machine Learning*, pages 2218–2227. PMLR, 2017.
- [16] Jakub M. Tomczak and Max Welling. Improving variational auto-encoders using householder flow. (arXiv:1611.09630), January 2017. URL <http://arxiv.org/abs/1611.09630>. arXiv:1611.09630 [cs, stat].

- [17] Jascha Sohl-Dickstein, Eric Weiss, Niru Maheswaranathan, and Surya Ganguli. Deep unsupervised learning using nonequilibrium thermodynamics. In Francis Bach and David Blei, editors, *Proceedings of the 32nd International Conference on Machine Learning*, volume 37 of *Proceedings of Machine Learning Research*, pages 2256–2265, Lille, France, 07–09 Jul 2015. PMLR. URL <https://proceedings.mlr.press/v37/sohl-dickstein15.html>.
- [18] Jonathan Ho, Ajay Jain, and Pieter Abbeel. Denoising diffusion probabilistic models. *Advances in neural information processing systems*, 33:6840–6851, 2020.
- [19] Yang Song and Stefano Ermon. Generative modeling by estimating gradients of the data distribution. *Advances in neural information processing systems*, 32, 2019.
- [20] Yang Song and Stefano Ermon. Improved techniques for training score-based generative models. *Advances in neural information processing systems*, 33:12438–12448, 2020.
- [21] Yang Song, Jascha Sohl-Dickstein, Diederik P Kingma, Abhishek Kumar, Stefano Ermon, and Ben Poole. Score-based generative modeling through stochastic differential equations. *arXiv preprint arXiv:2011.13456*, 2020.
- [22] Yang Song, Conor Durkan, Iain Murray, and Stefano Ermon. Maximum likelihood training of score-based diffusion models. *Advances in neural information processing systems*, 34:1415–1428, 2021.
- [23] Prafulla Dhariwal and Alexander Nichol. Diffusion models beat gans on image synthesis. *Advances in neural information processing systems*, 34:8780–8794, 2021.
- [24] Calvin Luo. Understanding diffusion models: A unified perspective. (arXiv:2208.11970), August 2022. URL <http://arxiv.org/abs/2208.11970>. arXiv:2208.11970 [cs].
- [25] Brian D.O. Anderson. Reverse-time diffusion equation models. *Stochastic Processes and their Applications*, 12(3):313–326, May 1982. ISSN 03044149. doi: 10.1016/0304-4149(82)90051-5.
- [26] Pascal Vincent. A connection between score matching and denoising autoencoders. *Neural Computation*, 23(7):1661–1674, 2011. doi: 10.1162/NECO_a_00142.
- [27] Peiran Gao, Eric Trautmann, Byron Yu, Gopal Santhanam, Stephen Ryu, Krishna Shenoy, and Surya Ganguli. *A theory of multineuronal dimensionality, dynamics and measurement*. November 2017. doi: 10.1101/214262. URL <http://biorxiv.org/lookup/doi/10.1101/214262>.
- [28] Tero Karras, Miika Aittala, Timo Aila, and Samuli Laine. Elucidating the design space of diffusion-based generative models. *Advances in Neural Information Processing Systems*, 35:26565–26577, 2022.
- [29] Diederik Kingma, Tim Salimans, Ben Poole, and Jonathan Ho. Variational diffusion models. *Advances in neural information processing systems*, 34:21696–21707, 2021.
- [30] Yaron Lipman, Ricky T Q Chen, Heli Ben-Hamu, Maximilian Nickel, and Matt Le. Flow matching for generative modeling. 2023.
- [31] Xingchao Liu, Chengyue Gong, and Qiang Liu. Flow straight and fast: Learning to generate and transfer data with rectified flow. 2023.
- [32] Michael S. Albergo and Eric Vanden-Eijnden. Building normalizing flows with stochastic interpolants. (arXiv:2209.15571), March 2023. URL <http://arxiv.org/abs/2209.15571>. arXiv:2209.15571 [cs, stat].
- [33] Michael S. Albergo, Nicholas M. Boffi, and Eric Vanden-Eijnden. Stochastic interpolants: A unifying framework for flows and diffusions. (arXiv:2303.08797), November 2023. URL <http://arxiv.org/abs/2303.08797>. arXiv:2303.08797 [cond-mat].
- [34] Alexander Tong, Kilian Fatras, Nikolay Malkin, Guillaume Hugué, Yanlei Zhang, Jarrid Rector-Brooks, Guy Wolf, and Yoshua Bengio. Improving and generalizing flow-based generative models with minibatch optimal transport. 2023. doi: 10.48550/ARXIV.2302.00482. URL <https://arxiv.org/abs/2302.00482>.

- [35] Aram-Alexandre Pooladian, Heli Ben-Hamu, Carles Domingo-Enrich, Brandon Amos, Yaron Lipman, and Ricky T. Q. Chen. Multisample flow matching: Straightening flows with minibatch couplings. (arXiv:2304.14772), May 2023. URL <http://arxiv.org/abs/2304.14772>. arXiv:2304.14772 [cs].
- [36] M Raphan and E P Simoncelli. Least squares estimation without priors or supervision. *Neural Computation*, 23(2):374–420, Feb 2011. doi: 10.1162/NECO_a_00076. Published online, Nov 2010.
- [37] Z Kadkhodaie and E P Simoncelli. Stochastic solutions for linear inverse problems using the prior implicit in a denoiser. In M. Ranzato, A. Beygelzimer, Y. Dauphin, P.S. Liang, and J. Wortman Vaughan, editors, *Adv. Neural Information Processing Systems (NeurIPS)*, volume 34, pages 13242–13254. Curran Associates, Inc., Dec 2021. URL https://proceedings.neurips.cc/paper_files/paper/2021/file/6e28943943dbed3c7f82fc05f269947a-Paper.pdf.
- [38] Yilun Xu, Ziming Liu, Max Tegmark, and Tommi Jaakkola. Poisson flow generative models. *Advances in Neural Information Processing Systems*, 35:16782–16795, 2022.
- [39] Yilun Xu, Ziming Liu, Yonglong Tian, Shangyuan Tong, Max Tegmark, and Tommi Jaakkola. Pfgm++: unlocking the potential of physics-inspired generative models. In *Proceedings of the 40th International Conference on Machine Learning, ICML’23*. JMLR.org, 2023.
- [40] Alan H Guth. Inflationary universe: A possible solution to the horizon and flatness problems. *Physical Review D*, 23(2):347, 1981.
- [41] Peter E Kloeden, Eckhard Platen, Peter E Kloeden, and Eckhard Platen. *Stochastic differential equations*. Springer, 1992.
- [42] Wenlong Mou, Nicolas Flammarion, Martin J Wainwright, and Peter L Bartlett. Improved bounds for discretization of langevin diffusions: Near-optimal rates without convexity. *Bernoulli*, 28(3):1577–1601, 2022.
- [43] Alex Krizhevsky, Geoffrey Hinton, et al. Learning multiple layers of features from tiny images. 2009.
- [44] Yunjey Choi, Youngjung Uh, Jaejun Yoo, and Jung-Woo Ha. Stargan v2: Diverse image synthesis for multiple domains. In *Proceedings of the IEEE Conference on Computer Vision and Pattern Recognition*, 2020.
- [45] https://anonymous.4open.science/r/Inflationary_Flows-61F1/.
- [46] Martin Heusel, Hubert Ramsauer, Thomas Unterthiner, Bernhard Nessler, and Sepp Hochreiter. Gans trained by a two time-scale update rule converge to a local nash equilibrium. In *Proceedings of the 31st International Conference on Neural Information Processing Systems, NIPS’17*, page 6629–6640, Red Hook, NY, USA, 2017. Curran Associates Inc. ISBN 9781510860964.
- [47] Zahra Kadkhodaie, Florentin Guth, Eero P Simoncelli, and Stéphane Mallat. Generalization in diffusion models arises from geometry-adaptive harmonic representations. In *The Twelfth International Conference on Learning Representations*, 2024. URL <https://openreview.net/forum?id=ANvmVS2Yr0>.
- [48] Chin-Wei Huang, Jae Hyun Lim, and Aaron C Courville. A variational perspective on diffusion-based generative models and score matching. *Advances in Neural Information Processing Systems*, 34:22863–22876, 2021.
- [49] Diederik P Kingma and Ruiqi Gao. Understanding diffusion objectives as the ELBO with simple data augmentation. In *Thirty-seventh Conference on Neural Information Processing Systems*, 2023. URL <https://openreview.net/forum?id=NnMEadcdyD>.
- [50] Nikolay Malkin, Salem Lahlou, Tristan Deleu, Xu Ji, Edward J Hu, Katie E Everett, Dinghuai Zhang, and Yoshua Bengio. GFlownets and variational inference. In *The Eleventh International Conference on Learning Representations*, 2023. URL <https://openreview.net/forum?id=uKiE0VIlUA->.

- [51] Zahra Kadkhodaie, Florentin Guth, Eero P Simoncelli, and Stéphane Mallat. Generalization in diffusion models arises from geometry-adaptive harmonic representations. In *The Twelfth International Conference on Learning Representations*, 2024. URL <https://openreview.net/forum?id=ANvmVS2Yr0>.
- [52] Berthy T. Feng, Jamie Smith, Michael Rubinstein, Huiwen Chang, Katherine L. Bouman, and William T. Freeman. Score-based diffusion models as principled priors for inverse imaging. In *2023 IEEE/CVF International Conference on Computer Vision (ICCV)*, page 10486–10497, Paris, France, October 2023. IEEE. ISBN 9798350307184. doi: 10.1109/ICCV51070.2023.00965. URL <https://ieeexplore.ieee.org/document/10377772/>.
- [53] Jiaming Song, Arash Vahdat, Morteza Mardani, and Jan Kautz. Pseudoinverse-guided diffusion models for inverse problems. In *International Conference on Learning Representations*, 2023. URL https://openreview.net/forum?id=9_gsMA8MRKQ.
- [54] Jiaming Song, Chenlin Meng, and Stefano Ermon. Denoising diffusion implicit models. In *International Conference on Learning Representations*, 2021. URL <https://openreview.net/forum?id=St1giarCHLP>.
- [55] Arpit Bansal, Eitan Borgnia, Hong-Min Chu, Jie Li, Hamid Kazemi, Furong Huang, Micah Goldblum, Jonas Geiping, and Tom Goldstein. Cold diffusion: Inverting arbitrary image transforms without noise. *Advances in Neural Information Processing Systems*, 36, 2024.
- [56] Severi Rissanen, Markus Heinonen, and Arno Solin. Generative modelling with inverse heat dissipation. In *The Eleventh International Conference on Learning Representations*, 2023. URL <https://openreview.net/forum?id=4PJUBT9f201>.
- [57] Emiel Hoogeboom and Tim Salimans. Blurring diffusion models. In *The Eleventh International Conference on Learning Representations*, 2023. URL <https://openreview.net/forum?id=0jDkC57x5sz>.
- [58] Julius Berner, Lorenz Richter, and Karen Ullrich. An optimal control perspective on diffusion-based generative modeling. *Transactions on Machine Learning Research*, 2024. ISSN 2835-8856. URL <https://openreview.net/forum?id=oYIjw37pTP>.
- [59] Lorenz Richter and Julius Berner. Improved sampling via learned diffusions. In *The Twelfth International Conference on Learning Representations*, 2024. URL <https://openreview.net/forum?id=h4pNR0s006>.
- [60] Francisco Vargas, Andrius Ovsianas, David Lopes Fernandes, Mark Girolami, Neil D Lawrence, and Nikolas Nüsken. Bayesian learning via neural schrödinger-föllmer flows. In *Fourth Symposium on Advances in Approximate Bayesian Inference*, 2022. URL <https://openreview.net/forum?id=1Fqd10N5yTF>.
- [61] Xunpeng Huang, Hanze Dong, Yifan HAO, Yian Ma, and Tong Zhang. Reverse diffusion monte carlo. In *The Twelfth International Conference on Learning Representations*, 2024. URL <https://openreview.net/forum?id=kIPEyMSdFV>.
- [62] Curtis McDonald and Andrew Barron. Proposal of a score based approach to sampling using monte carlo estimation of score and oracle access to target density. (arXiv:2212.03325), December 2022. doi: 10.48550/arXiv.2212.03325. URL <http://arxiv.org/abs/2212.03325>. arXiv:2212.03325 [cs, stat].
- [63] Angus Phillips, Hai-Dang Dau, Michael John Hutchinson, Valentin De Bortoli, George Deligiannidis, and Arnaud Doucet. Particle denoising diffusion sampler. (arXiv:2402.06320), February 2024. doi: 10.48550/arXiv.2402.06320. URL <http://arxiv.org/abs/2402.06320>. arXiv:2402.06320 [cs, stat].
- [64] Gabriel Cardoso, Yazid Janati el idrissi, Sylvain Le Corff, and Eric Moulines. Monte carlo guided denoising diffusion models for bayesian linear inverse problems. In *The Twelfth International Conference on Learning Representations*, 2024. URL <https://openreview.net/forum?id=nHESwVxwK>.

- [65] Brian L. Trippe, Luhuan Wu, Christian A. Naesseth, David Blei, and John Patrick Cunningham. Practical and asymptotically exact conditional sampling in diffusion models. In *ICML 2023 Workshop on Structured Probabilistic Inference & Generative Modeling*, 2023. URL <https://openreview.net/forum?id=r9s3Gbxz7g>.
- [66] Arash Vahdat, Karsten Kreis, and Jan Kautz. Score-based generative modeling in latent space. *Advances in neural information processing systems*, 34:11287–11302, 2021.
- [67] Andreas Blattmann, Robin Rombach, Huan Ling, Tim Dockhorn, Seung Wook Kim, Sanja Fidler, and Karsten Kreis. Align your latents: High-resolution video synthesis with latent diffusion models. In *Proceedings of the IEEE/CVF Conference on Computer Vision and Pattern Recognition*, pages 22563–22575, 2023.
- [68] Konpat Preechakul, Nattanat Chatthee, Suttisak Wizadwongsa, and Supasorn Suwajanakorn. Diffusion autoencoders: Toward a meaningful and decodable representation. In *Proceedings of the IEEE/CVF Conference on Computer Vision and Pattern Recognition*, pages 10619–10629, 2022.
- [69] Drew A Hudson, Daniel Zoran, Mateusz Malinowski, Andrew K Lampinen, Andrew Jaegle, James L McClelland, Loic Matthey, Felix Hill, and Alexander Lerchner. Soda: Bottleneck diffusion models for representation learning. *arXiv preprint arXiv:2311.17901*, 2023.
- [70] Bowen Jing, Gabriele Corso, Renato Berlinghieri, and Tommi Jaakkola. Subspace diffusion generative models. In *European Conference on Computer Vision*, pages 274–289. Springer, 2022.
- [71] Alexander Tong, Nikolay Malkin, Kilian Fatras, Lazar Atanackovic, Yanlei Zhang, Guillaume Huguet, Guy Wolf, and Yoshua Bengio. Simulation-free schrödinger bridges via score and flow matching. (arXiv:2307.03672), March 2024. URL <http://arxiv.org/abs/2307.03672>. arXiv:2307.03672 [cs].
- [72] Nataraj Akkiraju, Herbert Edelsbrunner, Michael Facello, Ping Fu, EP Mücke, and Carlos Varela. Alpha shapes: definition and software. In *Proceedings of the 1st international computational geometry software workshop*, volume 63, 1995.
- [73] Herbert Edelsbrunner and Ernst P Mücke. Three-dimensional alpha shapes. *ACM Transactions On Graphics (TOG)*, 13(1):43–72, 1994.
- [74] Fabian Pedregosa, Gaël Varoquaux, Alexandre Gramfort, Vincent Michel, Bertrand Thirion, Olivier Grisel, Mathieu Blondel, Peter Prettenhofer, Ron Weiss, Vincent Dubourg, et al. Scikit-learn: Machine learning in python. *Journal of machine learning research*, 12(Oct):2825–2830, 2011.

A Appendix: Additional Details on Model and Preliminaries

A.1 Derivation of the inflationary Fokker-Planck Equation

We start with derivatives of the smoothing kernel $\kappa(\mathbf{x}, t) \equiv \mathcal{N}(\mathbf{x}; \boldsymbol{\mu}, \mathbf{C}(t))$:

$$\partial_t \kappa(\mathbf{x}, t) = \left[-\frac{1}{2} \text{tr}(\mathbf{C}^{-1} \dot{\mathbf{C}}) + \frac{1}{2} \text{tr} \left(\mathbf{C}^{-1} (\mathbf{x} - \boldsymbol{\mu})(\mathbf{x} - \boldsymbol{\mu})^\top \mathbf{C}^{-1} \dot{\mathbf{C}} \right) \right] \kappa(\mathbf{x}, t) \quad (12)$$

$$\nabla \kappa = -\mathbf{C}^{-1} (\mathbf{x} - \boldsymbol{\mu}) \kappa \quad (13)$$

$$\partial_i \partial_j \kappa = \left[[\mathbf{C}^{-1} (\mathbf{x} - \boldsymbol{\mu})]_i [\mathbf{C}^{-1} (\mathbf{x} - \boldsymbol{\mu})]_j - (\mathbf{C}^{-1})_{ij} \right] \kappa \quad (14)$$

and combine this with (5) to calculate terms in (3):

$$\partial_t p = p_0(\mathbf{x}) * \partial_t \kappa(\mathbf{x}, t) \quad (15)$$

$$= p_0 * \left[-\frac{1}{2} \text{tr}(\mathbf{C}^{-1} \dot{\mathbf{C}}) + \frac{1}{2} \text{tr} \left(\mathbf{C}^{-1} (\mathbf{x} - \boldsymbol{\mu})(\mathbf{x} - \boldsymbol{\mu})^\top \mathbf{C}^{-1} \dot{\mathbf{C}} \right) \right] \kappa \quad (16)$$

$$- \sum_i \partial_i [f_i p] = -p_0 * \sum_i \left[(\partial_i f_i) \kappa - f_i (\mathbf{C}^{-1} (\mathbf{x} - \boldsymbol{\mu}))_i \kappa \right] \quad (17)$$

$$\begin{aligned} \frac{1}{2} \sum_{ij} \partial_i \partial_j \left[\sum_k G_{ik} G_{jk} p \right] &= \frac{1}{2} p_0 * \sum_{ij} \left[\partial_i \partial_j \left[\sum_k G_{ik} G_{jk} \right] \kappa \right. \\ &\quad \left. - 2 \partial_j \left[\sum_k G_{ik} G_{jk} \right] (\mathbf{C}^{-1} (\mathbf{x} - \boldsymbol{\mu}))_i \kappa \right. \\ &\quad \left. + \left[\sum_k G_{ik} G_{jk} \right] \left[[\mathbf{C}^{-1} (\mathbf{x} - \boldsymbol{\mu})]_i [\mathbf{C}^{-1} (\mathbf{x} - \boldsymbol{\mu})]_j - (\mathbf{C}^{-1})_{ij} \right] \kappa \right]. \end{aligned} \quad (18)$$

Assuming $\mathbf{f} = \mathbf{0}$ and $\partial_i G_{jk}(\mathbf{x}, t) = 0$ then gives the condition

$$\begin{aligned} -\frac{1}{2} \text{tr}(\mathbf{C}^{-1} \dot{\mathbf{C}}) + \frac{1}{2} \text{tr} \left(\mathbf{C}^{-1} (\mathbf{x} - \boldsymbol{\mu})(\mathbf{x} - \boldsymbol{\mu})^\top \mathbf{C}^{-1} \dot{\mathbf{C}} \right) &= \\ -\frac{1}{2} \text{tr}(\mathbf{C}^{-1} \mathbf{G} \mathbf{G}^\top) + \frac{1}{2} \text{tr} \left(\mathbf{C}^{-1} (\mathbf{x} - \boldsymbol{\mu})(\mathbf{x} - \boldsymbol{\mu})^\top \mathbf{C}^{-1} \mathbf{G} \mathbf{G}^\top \right) & \quad (19) \end{aligned}$$

which is satisfied when $\mathbf{G} \mathbf{G}^\top(\mathbf{x}, t) = \dot{\mathbf{C}}(t)$.

A.2 Stationary solutions of the inflationary Fokker-Planck Equation

Starting from the unscaled Fokker-Planck Equation corresponding to the process of Appendix A.1

$$\partial_t p_t(\mathbf{x}) = \frac{1}{2} \sum_{ij} \dot{C}_{ij}(t) \partial_i \partial_j p_t(\mathbf{x}), \quad (20)$$

we introduce new coordinates $\tilde{\mathbf{x}} = \mathbf{A}(t) \cdot \mathbf{x}$, $\tilde{t} = t$, leading to the change of derivatives

$$\partial_t = \frac{\partial \tilde{x}_i}{\partial t} \tilde{\partial}_i + \frac{\partial \tilde{t}}{\partial t} \tilde{\partial}_t \quad (21)$$

$$= \partial_t [A_{ij}(t) x_j] \tilde{\partial}_i + \tilde{\partial}_t \quad (22)$$

$$= [(\partial_t \mathbf{A}) \mathbf{A}^{-1} \tilde{\mathbf{x}}]_i \tilde{\partial}_i + \tilde{\partial}_t \quad (23)$$

$$\dot{C}_{ij} \partial_i \partial_j = \dot{C}_{ij} \frac{\partial \tilde{x}_k}{\partial x_i} \frac{\partial \tilde{x}_l}{\partial x_j} \tilde{\partial}_k \tilde{\partial}_l \quad (24)$$

$$= \dot{C}_{ij} A_{ki} A_{lj} \tilde{\partial}_k \tilde{\partial}_l \quad (25)$$

$$= (\mathbf{A} \dot{\mathbf{C}} \mathbf{A}^\top)_{kl} \tilde{\partial}_k \tilde{\partial}_l \quad (26)$$

and the Fokker-Planck Equation

$$\left[[(\partial_t \mathbf{A}) \mathbf{A}^{-1} \tilde{\mathbf{x}}]_i \tilde{\partial}_i + \tilde{\partial}_t \right] \tilde{p}_{\tilde{t}}(\tilde{\mathbf{x}}) = \frac{1}{2} (\mathbf{A} \dot{\mathbf{C}} \mathbf{A}^\top)_{kl} \tilde{\partial}_k \tilde{\partial}_l \tilde{p}_{\tilde{t}}(\tilde{\mathbf{x}}), \quad (27)$$

where $\tilde{p}_{\tilde{t}}(\tilde{\mathbf{x}}) = p_t(\mathbf{x})$ is simply written in rescaled coordinates. However, this is not a properly normalized probability distribution in the *rescaled* coordinates, so we define $q(\tilde{\mathbf{x}}, \tilde{t}) \equiv J^{-1}(\tilde{t}) \tilde{p}_{\tilde{t}}(\tilde{\mathbf{x}})$, which in turn satisfies

$$\left[[(\partial_t \mathbf{A}) \mathbf{A}^{-1} \tilde{\mathbf{x}}]_i \tilde{\partial}_i + \tilde{\partial}_t + \tilde{\partial}_t \log J \right] q(\tilde{\mathbf{x}}, \tilde{t}) = \frac{1}{2} (\mathbf{A} \dot{\mathbf{C}} \mathbf{A}^\top)_{kl} \tilde{\partial}_k \tilde{\partial}_l q(\tilde{\mathbf{x}}, \tilde{t}). \quad (28)$$

Now consider the time-dependent Gaussian density

$$q(\tilde{\mathbf{x}}, \tilde{t}) = \frac{1}{\sqrt{(2\pi)^{\frac{d}{2}} |\boldsymbol{\Sigma}| |\mathbf{A}^\top \mathbf{A}|}} \exp \left(-\frac{1}{2} (\tilde{\mathbf{x}} - \mathbf{A} \boldsymbol{\mu})^\top (\mathbf{A} \boldsymbol{\Sigma} \mathbf{A}^\top)^{-1} (\tilde{\mathbf{x}} - \mathbf{A} \boldsymbol{\mu}) \right) \quad (29)$$

with rescaling factor $J(\tilde{t}) = |\mathbf{A}^\top \mathbf{A}(t)|$. We then calculate the pieces of (28) as follows:

$$\begin{aligned} \tilde{\nabla} q &= -(\mathbf{A} \boldsymbol{\Sigma} \mathbf{A}^\top)^{-1} (\tilde{\mathbf{x}} - \mathbf{A} \boldsymbol{\mu}) q \\ \tilde{\partial}_i \tilde{\partial}_j q &= [(\mathbf{A} \boldsymbol{\Sigma} \mathbf{A}^\top)^{-1} (\tilde{\mathbf{x}} - \mathbf{A} \boldsymbol{\mu})]_i [(\mathbf{A} \boldsymbol{\Sigma} \mathbf{A}^\top)^{-1} (\tilde{\mathbf{x}} - \mathbf{A} \boldsymbol{\mu})]_j q - [(\mathbf{A} \boldsymbol{\Sigma} \mathbf{A}^\top)^{-1}]_{ij} q \\ \tilde{\partial}_t \log J &= \tilde{\partial}_t \log |\mathbf{A} \mathbf{A}^\top| = \text{tr}(\tilde{\partial}_t \log \mathbf{A} \mathbf{A}^\top) = \text{tr} \left((\mathbf{A} \mathbf{A}^\top)^{-1} \left[(\tilde{\partial}_t \mathbf{A}) \mathbf{A}^\top + \mathbf{A} (\tilde{\partial}_t \mathbf{A}^\top) \right] \right) \\ \tilde{\partial}_t q &= -\frac{1}{2} \text{tr}((\mathbf{A} \boldsymbol{\Sigma} \mathbf{A}^\top)^{-1} \tilde{\partial}_t (\mathbf{A} \boldsymbol{\Sigma} \mathbf{A}^\top)) q \\ &\quad + q \boldsymbol{\mu}^\top \tilde{\partial}_t \mathbf{A}^\top (\mathbf{A} \boldsymbol{\Sigma} \mathbf{A}^\top)^{-1} (\tilde{\mathbf{x}} - \mathbf{A} \boldsymbol{\mu}) \\ &\quad - \frac{q}{2} \text{tr} \left[(\tilde{\mathbf{x}} - \mathbf{A} \boldsymbol{\mu}) (\tilde{\mathbf{x}} - \mathbf{A} \boldsymbol{\mu})^\top \tilde{\partial}_t (\mathbf{A} \boldsymbol{\Sigma} \mathbf{A}^\top)^{-1} \right] \\ &\quad - \tilde{\partial}_t \log J \\ \tilde{\partial}_t (\mathbf{A} \boldsymbol{\Sigma} \mathbf{A}^\top)^{-1} &= -(\mathbf{A} \boldsymbol{\Sigma} \mathbf{A}^\top)^{-1} \tilde{\partial}_t (\mathbf{A} \boldsymbol{\Sigma} \mathbf{A}^\top) (\mathbf{A} \boldsymbol{\Sigma} \mathbf{A}^\top)^{-1} \\ &= -(\mathbf{A} \boldsymbol{\Sigma} \mathbf{A}^\top)^{-1} ((\tilde{\partial}_t \mathbf{A}) \mathbf{A}^{-1}) - ((\tilde{\partial}_t \mathbf{A}) \mathbf{A}^{-1})^\top (\mathbf{A} \boldsymbol{\Sigma} \mathbf{A}^\top)^{-1} \\ &\quad - \mathbf{A}^{-\top} \boldsymbol{\Sigma}^{-1} \tilde{\partial}_t \boldsymbol{\Sigma} \boldsymbol{\Sigma}^{-1} \mathbf{A}^{-1}. \end{aligned}$$

With these results, the left and right sides of (28) become

$$\begin{aligned} [\tilde{\mathbf{x}}^\top \cdot \tilde{\partial}_t \log \mathbf{A}^\top \cdot \tilde{\nabla} + \tilde{\partial}_t + \tilde{\partial}_t \log J] q &= -\tilde{\mathbf{x}}^\top [(\tilde{\partial}_t \mathbf{A}) \mathbf{A}^{-1}]^\top (\mathbf{A} \boldsymbol{\Sigma} \mathbf{A}^\top)^{-1} (\tilde{\mathbf{x}} - \mathbf{A} \boldsymbol{\mu}) q \\ &\quad - \frac{1}{2} \text{tr}((\mathbf{A} \boldsymbol{\Sigma} \mathbf{A}^\top)^{-1} \tilde{\partial}_t (\mathbf{A} \boldsymbol{\Sigma} \mathbf{A}^\top)) q \\ &\quad + \boldsymbol{\mu}^\top \tilde{\partial}_t \mathbf{A}^\top (\mathbf{A} \boldsymbol{\Sigma} \mathbf{A}^\top)^{-1} (\tilde{\mathbf{x}} - \mathbf{A} \boldsymbol{\mu}) q \\ &\quad - \frac{1}{2} \text{tr} \left((\tilde{\mathbf{x}} - \mathbf{A} \boldsymbol{\mu}) (\tilde{\mathbf{x}} - \mathbf{A} \boldsymbol{\mu})^\top \tilde{\partial}_t (\mathbf{A} \boldsymbol{\Sigma} \mathbf{A}^\top)^{-1} \right) q \\ &\quad - \tilde{\partial}_t \log |\mathbf{A} \mathbf{A}^\top| q \\ &\quad + \text{tr} \left((\mathbf{A} \mathbf{A}^\top)^{-1} \left[(\tilde{\partial}_t \mathbf{A}) \mathbf{A}^\top + \mathbf{A} (\tilde{\partial}_t \mathbf{A}^\top) \right] \right) q \\ &= -\frac{q}{2} \text{tr} \left(\tilde{\partial}_t (\mathbf{A} \boldsymbol{\Sigma} \mathbf{A}^\top) (\mathbf{A} \boldsymbol{\Sigma} \mathbf{A}^\top)^{-1} \right) \\ &\quad + \frac{q}{2} \text{tr} \left((\mathbf{A} \boldsymbol{\Sigma} \mathbf{A}^\top)^{-1} (\tilde{\mathbf{x}} - \mathbf{A} \boldsymbol{\mu}) (\tilde{\mathbf{x}} - \mathbf{A} \boldsymbol{\mu})^\top \left[\tilde{\partial}_t (\mathbf{A} \boldsymbol{\Sigma} \mathbf{A}^\top) (\mathbf{A} \boldsymbol{\Sigma} \mathbf{A}^\top)^{-1} \right] \right) \\ (\mathbf{A} \dot{\mathbf{C}} \mathbf{A}^\top)_{kl} \tilde{\partial}_k \tilde{\partial}_l q &= -\text{tr}(\mathbf{A} \dot{\mathbf{C}} \mathbf{A}^\top (\mathbf{A} \boldsymbol{\Sigma} \mathbf{A}^\top)^{-1}) q \\ &\quad + \text{tr} \left((\tilde{\mathbf{x}} - \mathbf{A} \boldsymbol{\mu})^\top (\mathbf{A} \boldsymbol{\Sigma} \mathbf{A}^\top)^{-1} (\mathbf{A} \dot{\mathbf{C}} \mathbf{A}^\top) (\mathbf{A} \boldsymbol{\Sigma} \mathbf{A}^\top)^{-1} (\tilde{\mathbf{x}} - \mathbf{A} \boldsymbol{\mu}) \right) q \end{aligned}$$

and $q(\tilde{\mathbf{x}}, \tilde{t})$ is a solution when

$$\begin{aligned} \frac{1}{2} \mathbf{A} \dot{\mathbf{C}} \mathbf{A}^\top (\mathbf{A} \boldsymbol{\Sigma} \mathbf{A}^\top)^{-1} &= \frac{1}{2} \tilde{\partial}_t (\mathbf{A} \boldsymbol{\Sigma} \mathbf{A}^\top) (\mathbf{A} \boldsymbol{\Sigma} \mathbf{A}^\top)^{-1} \\ \Rightarrow \mathbf{A} \dot{\mathbf{C}} \mathbf{A}^\top &= \tilde{\partial}_t (\mathbf{A} \boldsymbol{\Sigma} \mathbf{A}^\top). \end{aligned} \quad (30)$$

Thus, for q to be a solution in the absence of rescaling ($\mathbf{A} = \mathbb{1}$) requires $\dot{\Sigma} = \dot{\mathbf{C}}$, and combining this with (30) gives the additional constraint

$$\dot{\mathbf{A}}\Sigma\mathbf{A}^\top + \mathbf{A}\Sigma\dot{\mathbf{A}}^\top = \mathbf{0}. \quad (31)$$

Finally, note that, under the assumed form of $p_t(\mathbf{x})$ given in (5), when $\mathbf{C}(t)$ increases without bound, $q(\tilde{\mathbf{x}}, t) \rightarrow \mathcal{N}(\mathbf{0}, \mathbf{A}\mathbf{C}\mathbf{A}^\top(t))$ asymptotically (under rescaling), and this distribution is stationary when $\tilde{\Sigma}(t) = \mathbf{A}\Sigma\mathbf{A}^\top \rightarrow \mathbf{A}\mathbf{C}\mathbf{A}^\top$ is time-independent and a solution to (31).

A.3 Derivation of the inflationary pfODE

Here, we derive the form of the pfODE (6) in rescaled coordinates. Starting from the unscaled inflationary process (Appendix A.1) with $\mathbf{f} = \mathbf{0}$ and $\mathbf{G}\mathbf{G}^\top(\mathbf{x}, t) = \dot{\mathbf{C}}(t)$, substituting into (4) gives the pfODE

$$\frac{d\mathbf{x}}{dt} = -\frac{1}{2}\dot{\mathbf{C}}(t) \cdot \nabla_{\mathbf{x}} \log p_t(\mathbf{x}) \quad (32)$$

As in Appendix A.2, we again consider the rescaling transformation $\tilde{\mathbf{x}} = \mathbf{A}(t) \cdot \mathbf{x}$, $\tilde{t} = t$. To simplify the derivation, we start by parameterizing the particle trajectory using a worldline time τ such that $dt = d\tau$ while \mathbf{A} remains a function of t . With this convention, the pfODE becomes

$$\frac{d\tilde{x}_i}{d\tau} = \frac{\partial \tilde{x}_i}{\partial x_j} \frac{dx_j}{d\tau} + \frac{\partial \tilde{x}_i}{\partial t} \frac{dt}{d\tau} \quad (33)$$

$$= A_{ij} \frac{dx_j}{d\tau} + \frac{\partial(\mathbf{A}\mathbf{x})_i}{\partial t} \quad (34)$$

$$= A_{ij} \frac{dx_j}{d\tau} + \sum_{jk} (\partial_t A_{ij}) A_{jk}^{-1} A_{kl} x_l \Rightarrow \quad (35)$$

$$\frac{d\tilde{\mathbf{x}}}{d\tau} = \mathbf{A} \frac{d\mathbf{x}}{d\tau} + [(\partial_t \mathbf{A}) \mathbf{A}^{-1}] \cdot \tilde{\mathbf{x}} \quad (36)$$

$$= \mathbf{A} \cdot \left(-\frac{1}{2} \dot{\mathbf{C}} \cdot \nabla_{\mathbf{x}} \log p_t(\mathbf{x}) \right) + [(\partial_t \mathbf{A}) \mathbf{A}^{-1}] \cdot \tilde{\mathbf{x}}. \quad (37)$$

Two important things to note about this form: First, the score function $\nabla_{\mathbf{x}} \log p_t(\mathbf{x})$ is calculated in the *unscaled* coordinates. In practice, this is the form we use when integrating the pfODE, though the transformation to the scaled coordinates is straightforward. Second, the rescaling has induced a second force due to the change of measure factor, and this force points inward toward the origin when \mathbf{A} is a contraction. This overall attraction thus balances the repulsion from areas of high local density due to the negative score function, with the result that the asymptotic distribution is stabilized.

More formally, recalling the comments at the conclusion of Appendix A.2, when $\mathbf{C}(t)$ grows without bound in (5), $p_t(\mathbf{x})$, the unscaled density, is asymptotically Gaussian with covariance $\mathbf{C}(t)$, and its rescaled form $q(\tilde{\mathbf{x}}, \tilde{t})$ is a stationary solution of the corresponding rescaled Fokker-Planck Equation. In this case, we also have

$$\frac{d\tilde{\mathbf{x}}}{d\tau} \xrightarrow{t \rightarrow \infty} \left(\frac{1}{2} \mathbf{A} \dot{\mathbf{C}} \mathbf{C}^{-1} + \dot{\mathbf{A}} \right) \cdot \tilde{\mathbf{x}} = \mathbf{0}, \quad (38)$$

where we have made use of (31) with $\Sigma \rightarrow \mathbf{C}$. That is, when the rescaling and flow are chosen such that the (rescaled) diffusion PDE has a stationary Gaussian solution, points on the (rescaled) flow ODE eventually stop moving.

A.4 Equivalence of inflationary flows and standard pfODEs

Here, we show that our pfODE in (6) is equivalent to the form proposed by [28] for isotropic $\mathbf{C}(t)$ and $\mathbf{A}(t)$. We begin by taking equation (6) and rewriting it such that our score term is computed with respect to the rescaled variable $\tilde{\mathbf{x}}$:

$$\frac{d\tilde{\mathbf{x}}}{d\tilde{t}} = \mathbf{A} \cdot \left(-\frac{1}{2} \dot{\mathbf{C}} \cdot \mathbf{A}^\top \cdot \mathbf{s}_{\tilde{\mathbf{x}}}(\mathbf{A}^{-1} \tilde{\mathbf{x}}, \tilde{t}) \right) + [(\partial_t \mathbf{A}) \mathbf{A}^{-1}] \cdot \tilde{\mathbf{x}}, \quad (39)$$

where we have made use of the transformation properties of the score function under the rescaling.

If we then choose $\mathbf{C}(t) = c^2(t)\mathbb{1}$ and $\mathbf{A}(t) = \alpha(t)\mathbb{1}$ (i.e., isotropic noising and scaling schedules), this becomes

$$\frac{d\mathbf{x}}{dt} = -\alpha(t)^2 \dot{c}(t)c(t) \nabla_{\mathbf{x}} \log p\left(\frac{\mathbf{x}}{\alpha(t)}; t\right) + \frac{\dot{\alpha}(t)}{\alpha(t)} \mathbf{x}, \quad (40)$$

where we have dropped tildes on \mathbf{x} and t . This is exactly the same as the form given in Equation 4 of [28] if we substitute $\alpha(t) \rightarrow s(t)$, $c(t) \rightarrow \sigma(t)$.

A.5 Equivalence of inflationary flows and flow matching

Here, we show the equivalence of our proposed un-scaled (32) and scaled (37) pfODEs to the un-scaled and scaled ODEs obtained using the ‘‘Gaussian paths’’ flow matching formulation from [30]. Here, we will use the convention of the flow-matching literature in which $t = 0$ corresponds to the easily sampled distribution (e.g., Gaussian), while $t = 1$ corresponds to the target (data) distribution. In this setup, the flow $\mathbf{x}_t = \psi_t(\mathbf{x}_0)$ is likewise specified by an ODE:

$$\frac{d}{dt} \psi_t(\mathbf{x}_0) = \mathbf{v}_t(\psi_t(\mathbf{x}_0)|\mathbf{x}_1), \quad (41)$$

where again, \mathbf{x}_1 is a point in the data distribution and $\mathbf{x}_0 \sim \mathcal{N}(\mathbf{0}, \mathbb{1})$. In [30], the authors show that choosing

$$\mathbf{v}_t(\mathbf{x}|\mathbf{x}_1) = \frac{\dot{\sigma}_t(\mathbf{x}_1)}{\sigma_t(\mathbf{x}_1)} (\mathbf{x} - \boldsymbol{\mu}_t(\mathbf{x}_1)) + \dot{\boldsymbol{\mu}}_t(\mathbf{x}_1) \quad (42)$$

with ‘‘dots’’ denoting time derivatives leads to a flow

$$\psi_t(\mathbf{x}_0) = \sigma_t(\mathbf{x}_1) \mathbf{x}_0 + \boldsymbol{\mu}_t(\mathbf{x}_1), \quad (43)$$

that is, a conditionally linear transformation of the Gaussian sample \mathbf{x}_0 .

For our purposes, we can re-derive (42) for the general case where $\sigma_t(\mathbf{x}_1)$ is no longer a scalar but a matrix-valued function of \mathbf{x}_1 and time. That is, we rewrite (43) (equation 11 in [30]) with a full covariance matrix $\boldsymbol{\Sigma}_t(\mathbf{x}_1)$:

$$\mathbf{x}_t = \psi_t(\mathbf{x}_0) = \boldsymbol{\Sigma}_t^{\frac{1}{2}}(\mathbf{x}_1) \cdot \mathbf{x}_0 + \boldsymbol{\mu}_t(\mathbf{x}_1). \quad (44)$$

Similarly, we can write

$$\mathbf{v}_t(\mathbf{x}|\mathbf{x}_1) = \dot{\boldsymbol{\Sigma}}_t^{\frac{1}{2}}(\mathbf{x}_1) \boldsymbol{\Sigma}_t^{-\frac{1}{2}}(\mathbf{x}_1) \cdot (\mathbf{x} - \boldsymbol{\mu}_t(\mathbf{x}_1)) + \dot{\boldsymbol{\mu}}_t(\mathbf{x}_1), \quad (45)$$

from which it is straightforward to show that (41) is again satisfied.

This can be related to our pfODE (6) as follows: First, recall that, under the inflationary assumption (5) plus rescaling, our time-dependent *conditional* marginals are

$$p(\mathbf{x}_t|\mathbf{x}_1) = \mathcal{N}(\mathbf{A}_t \cdot \mathbf{x}_1, \mathbf{A}_t \mathbf{C}_t \mathbf{A}_t^\top), \quad (46)$$

which is equivalent to (44) with $\boldsymbol{\mu}_t(\mathbf{x}_1) = \mathbf{A}_t \cdot \mathbf{x}_1$, $\boldsymbol{\Sigma}_t(\mathbf{x}_1) = \mathbf{A}_t \mathbf{C}_t \mathbf{A}_t^\top$. Note that, here again, we have reversed our time conventions from the main paper to follow the flow-matching literature: $t = 0$ is our inflated Gaussian and $t = 1$ is the data distribution. From these results, along with the constraint (31) required for inflationary flows to produce a stationary Gaussian solution asymptotically, we then have, substituting into (45):

$$\dot{\boldsymbol{\Sigma}}_t^{\frac{1}{2}} \boldsymbol{\Sigma}_t^{-\frac{1}{2}} = \dot{\boldsymbol{\Sigma}}_t^{\frac{1}{2}} \boldsymbol{\Sigma}_t^{\frac{1}{2}} \boldsymbol{\Sigma}_t^{-1} = \frac{1}{2} \dot{\boldsymbol{\Sigma}}_t \boldsymbol{\Sigma}_t^{-1} \quad (47)$$

$$= \frac{1}{2} \mathbf{A}_t \dot{\mathbf{C}}_t \mathbf{A}_t^\top \boldsymbol{\Sigma}_t^{-1} \quad (48)$$

$$\Rightarrow \dot{\mathbf{x}}_t = \mathbf{v}_t(\mathbf{x}_t|\mathbf{x}_1) = \frac{1}{2} \mathbf{A}_t \dot{\mathbf{C}}_t \mathbf{A}_t^\top \boldsymbol{\Sigma}_t^{-1} \cdot (\mathbf{x}_t - \mathbf{A}_t \cdot \mathbf{x}_1) + \dot{\mathbf{A}}_t \cdot \mathbf{x}_1 \quad (49)$$

$$= -\frac{1}{2} \mathbf{A}_t \dot{\mathbf{C}}_t \mathbf{A}_t^\top \cdot \nabla_{\mathbf{x}_t} \log p(\mathbf{x}_t|\mathbf{x}_1) + \dot{\mathbf{A}}_t \mathbf{A}^{-1} \cdot \mathbf{x}_t, \quad (50)$$

which is the pfODE (6) written in the rescaled form (39). Thus, our inflationary flows are equivalent to a Gaussian paths flow matching approach for a particular choice of (matrix-valued) noise schedule and mean.

A.6 Derivation of dimension-preserving criterion

Here, for simplicity of notation, denote the participation ratio (7) by $R(\boldsymbol{\Sigma})$ and let $\boldsymbol{\Sigma} = \text{diag}(\boldsymbol{\gamma})$ in its eigenbasis, so that

$$R(\boldsymbol{\gamma}) = \frac{(\sum_i \gamma_i)^2}{\sum_j \gamma_j^2} \quad (51)$$

and the change in PR under a change in covariance is given by

$$dR(\boldsymbol{\gamma}) = 2 \frac{\sum_i \gamma_i}{\sum_j \gamma_j^2} \sum_k d\gamma_k - \frac{(\sum_i \gamma_i)^2}{(\sum_j \gamma_j^2)^2} \sum_k \gamma_k d\gamma_k \quad (52)$$

$$= 2 \frac{\sum_i \gamma_i}{\sum_i \gamma_i^2} \left(\mathbf{1} - R(\boldsymbol{\gamma}) \frac{\boldsymbol{\gamma}}{\sum_i \gamma_i} \right) \cdot d\boldsymbol{\gamma}. \quad (53)$$

Requiring that PR be preserved ($dR = 0$) then gives (8).

Now, we would like to consider conditions under which PR is not preserved (i.e., (8) does not hold). Assume we are given $\dot{\boldsymbol{\gamma}}(t)$ (along with initial conditions $\boldsymbol{\gamma}(0)$) and define

$$\mathcal{R}(t) \equiv \frac{(\sum_i \gamma_i)(\sum_j \dot{\gamma}_j)}{\sum_k \gamma_k \dot{\gamma}_k} \quad (54)$$

so that

$$\left(\mathbf{1} - \mathcal{R}(t) \frac{\boldsymbol{\gamma}}{\sum_i \gamma_i} \right) \cdot \dot{\boldsymbol{\gamma}} = 0 \quad (55)$$

by definition. Then we can rewrite (8) as

$$\begin{aligned} \frac{dR(\boldsymbol{\gamma})}{dt} &= 2 \frac{\sum_i \gamma_i}{\sum_i \gamma_i^2} \left(\mathbf{1} - \mathcal{R}(t) \frac{\boldsymbol{\gamma}}{\sum_i \gamma_i} \right) \cdot \dot{\boldsymbol{\gamma}} - 2(R(\boldsymbol{\gamma}) - \mathcal{R}(t)) \frac{\boldsymbol{\gamma}}{\sum_i \gamma_i^2} \cdot \dot{\boldsymbol{\gamma}} \\ &= 0 - (R(\boldsymbol{\gamma}) - \mathcal{R}(t)) \frac{d}{dt} (\log \sum_i \gamma_i^2) \\ &= -(R(\boldsymbol{\gamma}) - \mathcal{R}(t)) \frac{d}{dt} (\log \text{Tr}(\mathbf{C}^2)). \end{aligned} \quad (56)$$

In the cases we consider, flows are *expansive* ($d(\log \text{Tr}(\mathbf{C}^2)) > 0$), with the result that (56) drives $R(\boldsymbol{\gamma})$ toward $\mathcal{R}(t)$. Thus, in cases where $\mathcal{R}(t)$ has an asymptotic value, the $R(\boldsymbol{\gamma})$ should approach this value as well. In particular, for our dimension-reducing flows, we have $\boldsymbol{\gamma} = \rho \mathbf{g} \odot \boldsymbol{\gamma}$, giving

$$\mathcal{R}(t) = \frac{(\sum_i \gamma_i)(\rho \sum_j g_j \dot{\gamma}_j)}{\rho \sum_k g_k \dot{\gamma}_k^2} \xrightarrow{t \rightarrow \infty} \frac{(\sum_{i=1}^K \gamma_{0i})^2}{\sum_{k=1}^K \gamma_{0k}^2}, \quad (57)$$

where $i = 1 \dots K$ are the dimensions with $g_i = g_*$ and $\gamma_k(0) = \gamma_{0k}$. That is, the asymptotic value of $\mathcal{R}(t)$ (and thus the asymptotic value of PR) is that of the covariance in which only the eigendimensions with $g_k = g_*$ have been retained, as in (10).

B Appendix: Additional Details on Model Training and Experiments

B.1 Derivation of Training preconditioning Terms

Following an extensive set of experiments, the authors of [28] propose a set of preconditioning factors for improving the efficiency of denoiser training (11) that forms the core of score estimation. More specifically, they parameterize the denoiser network $\mathbf{D}_\theta(\mathbf{x}; \sigma)$ as

$$\mathbf{D}_\theta(\mathbf{x}, \sigma) = c_{skip}(\sigma)\mathbf{x} + c_{out}(\sigma)\mathbf{F}_\theta(c_{in}(\sigma)\mathbf{x}; c_{noise}(\sigma)), \quad (58)$$

where \mathbf{F}_θ is the actual neural network being trained and c_{in} , c_{out} , c_{skip} , and c_{noise} are preconditioning factors. Using this parameterization of $\mathbf{D}_\theta(\mathbf{x}; \sigma)$, they then re-write the original L_2 de-noising loss as

$$\mathcal{L}(\mathbf{D}_\theta) = \mathbb{E}_{\sigma, \mathbf{y}, \mathbf{n}} \left[w(\sigma) \left\| \mathbf{F}_\theta(c_{in} \cdot (\mathbf{y} + \mathbf{n}); c_{noise}(\sigma)) - \frac{1}{c_{out}} (\mathbf{y} - c_{skip}(\sigma) \cdot (\mathbf{y} + \mathbf{n})) \right\|_2^2 \right], \quad (59)$$

where $w(\sigma)$ is also a preconditioning factor, \mathbf{y} is the original data sample, \mathbf{n} is a noise sample and $\mathbf{x} = \mathbf{y} + \mathbf{n}$. As detailed in [28], these "factors" stabilize DBM training by:

1. c_{in} : Scaling inputs to unit variance across all dimensions, and for all noise/perturbation levels. This is essential for stable neural net training via gradient descent.
2. c_{out} : Scaling the effective network output to unit variance across dimensions.
3. c_{skip} : Compensating for c_{out} , thus ensuring network errors are minimally amplified. The authors of [28] point out that this factor allows the network to choose whether to predict the target, its residual, or some value between the two.
4. $w(\sigma)$: Uniformizing the weight given to different noise levels in the total loss.
5. c_{noise} : Determining how noise levels should be sampled during training so that the trained network efficiently covers different noise levels. This is the conditioning noise input fed to the network along with the perturbed data. This quantity is determined empirically.

In [28], the authors propose optimal forms for all of these quantities based on these plausible first principles (cf. Table 1 and Appendix B.6 of that work). However, the forms proposed there rely strongly on the assumption that the noise schedule is isotropic, which does not hold for our inflationary schedules, which are diagonal but not proportional to the identity. Here, we derive analogous expressions for our setting.

As in the text, assume we work in the eigenbasis of the initial data distribution Σ_0 and let $\mathbf{C}(t) = \text{diag}(\gamma(t))$ be the noising schedule, such that the data covariance at time t is $\Sigma(t) = \Sigma_0 + \mathbf{C}(t)$. Assuming a noise-dependent weighting factor $\Lambda(t)$ analogous to $\sqrt{w(\sigma)}$ above, we then rewrite (11) as

$$\mathcal{L}(\mathbf{D}_\theta) = \mathbb{E}_{\mathbf{t}, \mathbf{y}, \mathbf{n}} \left[\|\Lambda(t)(\mathbf{D}_\theta(\mathbf{y} + \mathbf{n}; \gamma(t)) - \mathbf{y})\|^2 \right] \quad (60)$$

$$= \mathbb{E}_{\mathbf{t}, \mathbf{y}, \mathbf{n}} \left[\|\Lambda(t) (\mathbf{C}_{out} \mathbf{F}_\theta(\mathbf{C}_{in}(\mathbf{y} + \mathbf{n}); \mathbf{c}_{noise}) - (\mathbf{y} - \mathbf{C}_{skip}(\mathbf{y} + \mathbf{n})))\|^2 \right] \quad (61)$$

$$= \mathbb{E}_{\mathbf{t}, \mathbf{y}, \mathbf{n}} \left[\|\Lambda(t) \mathbf{C}_{out} (\mathbf{F}_\theta(\mathbf{C}_{in}(\mathbf{y} + \mathbf{n}); \mathbf{c}_{noise}) - \mathbf{C}_{out}^{-1}(\mathbf{y} - \mathbf{C}_{skip}(\mathbf{y} + \mathbf{n})))\|^2 \right] \quad (62)$$

This clearly generalizes (59) by promoting all preconditioning factors either to matrices (\mathbf{C}_{in} , \mathbf{C}_{out} , \mathbf{C}_{skip} , Λ) or vectors (\mathbf{c}_{noise}). We now derive forms for each of these preconditioning factors.

B.1.1 \mathbf{C}_{in}

The goal is to choose \mathbf{C}_{in} such that its application to the noised input $\mathbf{y} + \mathbf{n}$ has unit covariance:

$$\mathbb{1} = \text{Var}_{\mathbf{y}, \mathbf{n}} [\mathbf{C}_{in}(\mathbf{y} + \mathbf{n})] \quad (63)$$

$$= \mathbf{C}_{in} \text{Var}_{\mathbf{y}, \mathbf{n}} [(\mathbf{y} + \mathbf{n})] \mathbf{C}_{in}^\top \quad (64)$$

$$= \mathbf{C}_{in} (\Sigma_0 + \mathbf{C}(t)) \mathbf{C}_{in}^\top \quad (65)$$

$$= \mathbf{C}_{in} \Sigma(t) \mathbf{C}_{in}^\top \quad (66)$$

$$\Rightarrow \mathbf{C}_{in} = \Sigma^{-\frac{1}{2}}(t) \quad (67)$$

More explicitly, if \mathbf{W} is the matrix whose columns are the eigenvectors of Σ_0 , then

$$\mathbf{C}_{\text{in}} = \mathbf{W} \text{diag} \left(1/\sqrt{\sigma_0^2 + \gamma(t)} \right) \mathbf{W}^\top, \quad (68)$$

where the square root is taken elementwise.

B.1.2 $\mathbf{C}_{\text{out}}, \mathbf{C}_{\text{skip}}$

We begin by imposing the requirement that the target for the neural network \mathbf{F} should have identity covariance:

$$\mathbb{1} = \text{Var}_{\mathbf{y}, \mathbf{n}} [\mathbf{C}_{\text{out}}^{-1}(\mathbf{y} - \mathbf{C}_{\text{skip}}(\mathbf{y} + \mathbf{n}))] \quad (69)$$

$$\begin{aligned} \Rightarrow \mathbf{C}_{\text{out}} \mathbf{C}_{\text{out}}^\top &= \text{Var}_{\mathbf{y}, \mathbf{n}} [\mathbf{y} - \mathbf{C}_{\text{skip}}(\mathbf{y} + \mathbf{n})] \\ &= \text{Var}_{\mathbf{y}, \mathbf{n}} [(\mathbb{1} - \mathbf{C}_{\text{skip}})\mathbf{y} - \mathbf{C}_{\text{skip}}\mathbf{n}] \\ &= (\mathbb{1} - \mathbf{C}_{\text{skip}})\Sigma_0(\mathbb{1} - \mathbf{C}_{\text{skip}})^\top + \mathbf{C}_{\text{skip}}\mathbf{C}(t)\mathbf{C}_{\text{skip}}^\top. \end{aligned} \quad (70)$$

This generalizes Equation 123 in Appendix B.6 of [28].

Again by analogy with [28], we choose \mathbf{C}_{skip} to minimize the left-hand side of (70):

$$\mathbf{0} = -(\mathbb{1} - \mathbf{C}_{\text{skip}})\Sigma_0 + \mathbf{C}_{\text{skip}}\mathbf{C}(t) \quad (71)$$

$$\Rightarrow \Sigma_0 = \mathbf{C}_{\text{skip}}\Sigma(t) \quad (72)$$

$$\Rightarrow \mathbf{C}_{\text{skip}} = \Sigma_0 \Sigma^{-1}(t) = \mathbf{W} \text{diag} (\sigma_0^2 / (\sigma_0^2 + \gamma(t))) \mathbf{W}^\top, \quad (73)$$

which corresponds to Equation 131 in Appendix B.6 of [28].

Using (73) in (70) then allows us to solve for \mathbf{C}_{out} :

$$\mathbf{C}_{\text{out}} \mathbf{C}_{\text{out}}^\top = (\mathbb{1} - \Sigma_0 \Sigma^{-1})\Sigma_0(\mathbb{1} - \Sigma_0 \Sigma^{-1})^\top + \Sigma_0 \Sigma^{-1} \mathbf{C} \Sigma^{-1} \Sigma_0 \quad (74)$$

$$= \Sigma_0 - 2\Sigma_0 \Sigma^{-1} \Sigma_0 + \Sigma_0 \Sigma^{-1} (\Sigma_0 + \mathbf{C}) \Sigma^{-1} \Sigma_0 \quad (75)$$

$$= \Sigma_0 - \Sigma_0 \Sigma^{-1} \Sigma_0 \quad (76)$$

$$= \left(\Sigma_0^{-1} + \mathbf{C}^{-1}(t) \right)^{-1} \quad (77)$$

$$\Rightarrow \mathbf{C}_{\text{out}} = \mathbf{W} \text{diag} \left(\sqrt{\sigma_0^2 \odot \gamma(t) / (\sigma_0^2 + \gamma(t))} \right) \mathbf{W}^\top \quad (78)$$

B.1.3 $\Lambda(t)$

Our goal in choosing $\Lambda(t)$ is to equalize the loss across different noise levels (which correspond, via the noise schedule, to different times). Looking at the form of (62), we can see that this will be satisfied when $\Lambda(t)$ is chosen to cancel the outermost factor of \mathbf{C}_{out}

$$\Lambda(t) = \mathbf{C}_{\text{out}}^{-1} = \Sigma_0^{-1} + \mathbf{C}^{-1}(t) = \mathbf{W} \text{diag} \left(\sqrt{\sigma_0^{-2} + \gamma^{-1}(t)} \right) \mathbf{W}^\top \quad (79)$$

B.1.4 Re-writing loss with optimal preconditioning factors

Using these results, we now rewrite (62) using the preconditioning factors derived above:

$$\begin{aligned} \mathcal{L}(\mathbf{D}_\theta) &= \mathbb{E}_{\mathbf{t}, \mathbf{y}, \mathbf{n}} [\| \Lambda(t) \mathbf{C}_{\text{out}} (\mathbf{F}_\theta(\mathbf{C}_{\text{in}}(\mathbf{y} + \mathbf{n}); \mathbf{c}_{\text{noise}}) - \mathbf{C}_{\text{out}}^{-1}(\mathbf{y} - \mathbf{C}_{\text{skip}}(\mathbf{y} + \mathbf{n}))) \|^2] \\ &= \mathbb{E}_{\mathbf{t}, \mathbf{y}, \mathbf{n}} \left[\left\| \mathbf{F}_\theta(\Sigma^{-\frac{1}{2}}(t) \cdot (\mathbf{y} + \mathbf{n}); \mathbf{c}_{\text{noise}}) - \left(\Sigma_0^{-1} + \mathbf{C}^{-1}(t) \right)^{\frac{1}{2}} \cdot (\mathbf{y} - \Sigma_0 \Sigma^{-1}(t) \cdot (\mathbf{y} + \mathbf{n})) \right\|^2 \right]. \end{aligned}$$

In practice, we precompute \mathbf{W} and σ_0^2 via SVD and compute all relevant preconditioners in eigenspace using the forms given above. For $\mathbf{c}_{\text{noise}}$, we follow the same noise conditioning scheme used in the DDPM model [18], sampling t uniformly from some interval $t \sim \mathcal{U}[t_{\text{min}}, t_{\text{max}}]$ and then setting $c_{\text{noise}} = (M - 1)t$, for some scalar hyperparameter M . We choose $M = 1000$, in agreement with [28, 18]. After this, as indicated above, our noise is sampled via $\mathbf{n} \sim \mathcal{N}(\mathbf{0}, \mathbf{C}(t))$ with $\mathbf{C}(t) = \mathbf{W} \text{diag}(\gamma(t)) \mathbf{W}^\top$.

B.2 Construction of \mathbf{g} and its impact on compression and generative performance of PR-Reducing pFODEs

To construct \mathbf{g} in our PR-Reducing experiments, we chose to make all elements of \mathbf{g} corresponding to preserved dimensions equal to 2 (i.e., $g_{\text{preserved_dims}} = g_{\text{max}} = 2$) and all elements corresponding to compressed dimensions equal to $g_{\text{compressed_dims}} = g_{\text{min}} = 1 - \frac{d}{(D-d)}$, where d is the number of dimensions being preserved and D is total number of dimensions. Note that, using this construction, PR-Reducing schedules with a higher number of preserved dimensions d have a smaller value of \mathbf{g} for compressed dimensions, for a given fixed D . As such, PR-Preserving networks with higher d are exposed to a higher noise range ratio (i.e., higher $e^{\rho(g_{\text{max}}-g_{\text{min}})t}$) during training and need to optimally amortize score estimation over this wider ‘‘inflation gap,’’ which is a *harder* learning problem. This is confirmed empirically by looking at the results of our Frechet Inception Distance (FID) [46] and round-trip mean squared error (MSE) experiments (Table 1), which show that PR-Reducing networks with higher number of preserved dimensions and, therefore, wider inflation gaps, have higher FID scores and MSEs.

We present values for $g_{\text{preserved_dims}}$ and $g_{\text{compressed_dims}}$ constructed using the prescription above for our toy and image experiments in Appendix B.4. Additionally, in Tables 3 and 7, we show the latent space variances achieved at the end of inflation for compressed dimensions across the different PR-Reducing regimes investigated here (i.e., PR-Reducing to 1D or 2D, for toys, and PR-Reducing (PRR) to 2%, 10%, and 20% of nominal dimensions, for images). Note that, as expected, the schedules with wider ‘‘exponential inflation gap’’ (i.e., PR-Reducing to 2D (toys) or to 20% (images)) achieve the highest effective compression (lowest latent space variance for compressed dimensions). Therefore, for our specific \mathbf{g} construction scheme, actual compression achieved should be understood *both* in terms of number of dimensions preserved and in terms of effective latent space variance (for compressed dimensions) achieved at the end of inflation.

B.3 Details of pFODE integration

B.3.1 pFODE in terms of network outputs

Here we rewrite the pFODE (6) in terms of the network outputs $\mathbf{D}(\mathbf{x}, \text{diag}(\boldsymbol{\gamma}(t)))$, learned during training and queried in our experiments. As described in Appendix B.1.4 and in line with previous DBM training approaches, we opt to use time directly as our network conditioning input. That is, our networks are parameterized as $\mathbf{D}(\mathbf{x}, t)$. Then, using the fact that the score can be written in terms of the network as [21, 28]

$$\nabla_{\mathbf{x}} \log p(\mathbf{x}, \mathbf{C}(t)) = \mathbf{C}^{-1}(t) \cdot (\mathbf{D}(\mathbf{x}, t) - \mathbf{x}), \quad (80)$$

we rewrite (6) as

$$\frac{d\tilde{\mathbf{x}}}{dt} = -\frac{1}{2} \mathbf{A} \dot{\mathbf{C}} [\mathbf{C}^{-1}(\mathbf{D}(\mathbf{x}, t) - \mathbf{x})] + [(\partial_t \mathbf{A}) \mathbf{A}^{-1}] \cdot \tilde{\mathbf{x}} \quad (81)$$

$$= -\frac{1}{2} \mathbf{A} \dot{\mathbf{C}} [\mathbf{C}^{-1}(\mathbf{D}(\mathbf{A}^{-1} \cdot \tilde{\mathbf{x}}, t) - \mathbf{A}^{-1} \cdot \tilde{\mathbf{x}})] + [(\partial_t \mathbf{A}) \mathbf{A}^{-1}] \cdot \tilde{\mathbf{x}} \quad (82)$$

$$= -\frac{1}{2} \boldsymbol{\alpha}(t) \odot \frac{\dot{\boldsymbol{\gamma}}(t)}{\boldsymbol{\gamma}(t)} \odot \left(\mathbf{D} \left(\frac{\tilde{\mathbf{x}}}{\boldsymbol{\alpha}(t)}, t \right) - \frac{\tilde{\mathbf{x}}}{\boldsymbol{\alpha}(t)} \right) + \frac{\dot{\boldsymbol{\alpha}}(t)}{\boldsymbol{\alpha}(t)} \odot \tilde{\mathbf{x}}, \quad (83)$$

where in the last line we have expressed $\mathbf{A}(t)$ and $\dot{\mathbf{C}}\mathbf{C}^{-1}$ in their respective eigenspace (diagonal) representations, where the divisions are to be understood element-wise. For PR-Reducing schedules, this expression simplifies even further, since our scaling schedule becomes isotropic - i.e., $\mathbf{A}(t) = \alpha(t)\mathbb{1}$.

B.3.2 Solvers and Discretization Schedules

To integrate (83), we utilize either Euler’s method for toy datasets and Heun’s method (see **Algorithm 1**) for high-dimensional image datasets. The latter has been shown to provide better tradeoffs between number of neural function evaluations (NFEs) and image quality as assessed through FID scores in larger data sets [28].

In toy data examples, we chose a simple, linearly spaced (step size $h = 10^{-2}$) discretization scheme, integrating from $t = 0$ to $t = t_{\text{max}}$ when inflating and reversing these endpoints when generating

data from the latent space. For higher-dimensional image datasets (CIFAR-10, AFHQv2), we instead discretized using $t_i = \frac{i}{N-1}(t_{max} - \epsilon_s) + \epsilon_s$ when inflating, where t_{max} is again the maximum time at which networks were trained to denoise and $\epsilon_s = 10^{-2}$, similar to the standard discretization scheme for VP-ODEs [28, 21] (though we do not necessarily enforce $t_{max} = 1$). When generating from latent space, this discretization is preserved but integration is performed in reverse.

Algorithm 1 Eigen-Basis pfODE Simulation using Heun’s 2^{nd} order method

```

1: procedure HEUNSAMPLER( $\mathbf{D}_\theta(\mathbf{x}, t)$ ,  $\gamma(t)$ ,  $\alpha(t)$ ,  $\mathbf{W}^\top$ ,  $t_i \in \{0, \dots, N\}$ )
2:   if running "generation" then                                     ▷ Generate initial sample at  $t_0$ 
3:      $\tilde{\mathbf{x}}_0 \sim \mathcal{N}(\mathbf{0}, \text{diag}(\alpha(t_0) \odot \gamma(t_0)))$              ▷ Sample from Gaussian latent space
4:   else                                                             ▷ i.e., if running "inflation"
5:      $\mathbf{x}_0 \sim p_{data}(\mathbf{x})$                                        ▷ Sample from target distribution
6:      $\tilde{\mathbf{x}}_0 = \alpha(t_0)(\mathbf{W}^\top \cdot \mathbf{x}_0)$                              ▷ Transform to eigenbasis, scale
7:   end if
8:   for  $i \in \{0, 1, \dots, N - 1\}$  do:                               ▷ Solve equation (83)  $N$  times
9:      $\tilde{\mathbf{d}}_i \leftarrow -\frac{1}{2}\alpha(t_i) \odot \frac{\dot{\gamma}(t_i)}{\gamma(t_i)} \odot \left( \mathbf{D} \left( \frac{\tilde{\mathbf{x}}_i}{\alpha(t_i)}, t_i \right) - \frac{\tilde{\mathbf{x}}_i}{\alpha(t_i)} \right)$ 
10:     $+ \frac{\dot{\alpha}(t_i)}{\alpha(t_i)} \odot \tilde{\mathbf{x}}_i$                                      ▷ Evaluate  $\frac{d\tilde{\mathbf{x}}}{dt}$  at  $t_i$ 
11:     $\tilde{\mathbf{x}}_{i+1} \leftarrow \tilde{\mathbf{x}}_i + (t_{i+1} - t_i)\tilde{\mathbf{d}}_i$ ,  $\mathbf{x}_{i+1} = \frac{\tilde{\mathbf{x}}_{i+1}}{\alpha(t_{i+1})}$    ▷ Take Euler step from  $t_i$  to  $t_{i+1}$ 
12:     $\tilde{\mathbf{d}}'_i \leftarrow -\frac{1}{2}\alpha(t_{i+1}) \odot \frac{\dot{\gamma}(t_{i+1})}{\gamma(t_{i+1})} \odot \left( \mathbf{D} \left( \frac{\tilde{\mathbf{x}}_{i+1}}{\alpha(t_{i+1})}, t_{i+1} \right) - \frac{\tilde{\mathbf{x}}_{i+1}}{\alpha(t_{i+1})} \right)$ 
13:     $+ \frac{\dot{\alpha}(t_{i+1})}{\alpha(t_{i+1})} \odot \tilde{\mathbf{x}}_{i+1}$                              ▷ Evaluate  $\frac{d\tilde{\mathbf{x}}}{dt}$  at  $t_{i+1}$ 
14:     $\tilde{\mathbf{x}}_{i+1} \leftarrow \tilde{\mathbf{x}}_i + (t_{i+1} - t_i) \left( \frac{1}{2}\tilde{\mathbf{d}}_i + \frac{1}{2}\tilde{\mathbf{d}}'_i \right)$    ▷ Apply trapezoidal rule at  $t_{i+1}$ 
15:   return  $\tilde{\mathbf{x}}_N$                                                  ▷ Return Sample
16: end procedure

```

B.4 Training Details

B.4.1 Toy DataSets

Toy models were trained using a smaller convolutional UNet architecture (*ToyConvUNet*) and our proposed preconditioning factors (Appendix B.1). For all toy datasets, we trained networks both by using original images as inputs (i.e., “image space basis”) or by first transforming images to their PCA representation (i.e., “eigenbasis”). Networks trained using either base choice were able to produce qualitatively good generated samples, across all datasets. For all cases, we used $\rho = 1$, a learning rate of 10^{-5} , batch size of 8192, and exponential moving average half-life of 50×10^4 . Additionally, for PR-Reducing schedules, we chose $g_{preserved_dims} = 2$ (all datasets), and $g_{compressed_dims} = 0$ (2D datasets), or $g_{compressed_dims} = -1$ (3D datasets) (cf. Appendix B.2). The only exceptions were networks used on mesh/ 2D alpha-shape toy experiments, where we used instead $g_{preserved_dims} = 1.15$ across all preserved dimensions (circles, S-curve) and $g_{compressed_dims} = 0.85$ (circles), or $g_{compressed_dims} = 0.70$ (S-curve). This yields a softer effective compression (i.e., smaller “inflation gap”) and is needed to avoid numerical underflow errors when fitting meshes or 2D alpha-shapes to the compressed latent spaces (see Appendix B.6).

Table 2: Toy Data Training Hyperparameters

Dataset	Schedule	Total Dimensions	Dimensions Kept	t_{\max} (s)	Duration (Mimg)
Circles	PRP	2	2	7.01	6975
Circles	PRR	2	1	11.01	8601
Sine	PRP	2	2	7.01	12288
Sine	PRR	2	1	11.01	12288
Moons	PRP	2	2	8.01	6400
Moons	PRR	2	1	11.01	8704
S Curve	PRP	3	3	9.01	6144
S Curve	PRR	3	2	15.01	5160
Swirl	PRP	3	3	11.01	8704
Swirl	PRR	3	2	15.01	12042

Table 3: Toy Experiments Latent Space Compressed Dimension Variance

Dataset	Schedule	Dimensions Kept	Latent Space Compressed Dimension Variance
Circles	PRR	1	4×10^{-7}
Sine	PRR	1	4×10^{-7}
Moons	PRR	1	4×10^{-7}
S Curve	PRR	2	2×10^{-12}
Swirl	PRR	2	2×10^{-12}

As explained in Appendix B.1, to construct our \mathbf{c}_{noise} preconditioning factor, we sampled $t \sim \mathcal{U}(t_{min}, t_{max})$, with $t_{min} = 10^{-7}$ across all simulations and t_{max} equal to the values shown in Table 2. In the same table, we also show training times (in millions of images (Mimgs, as in [28])), along with both the total number of dimensions (in the original data) and the number of dimensions preserved (in latent space) for each dataset and schedule combination. In Table 3, we showcase latent space (i.e., end of “inflation”) compressed dimension variances achieved for the different toy PR-Reducing experiments.

B.4.2 CIFAR-10 and AFHQv2 Datasets

For our image datasets (i.e., CIFAR-10 and AFHQv2), we utilized similar training hyperparameters to the ones proposed by [28] for the CIFAR-10 dataset, across all schedules (e.g., PR-Preserving (PRP), PR-Reducing (PRR) to 2, 10, and 20%) (Table 4). Shown in Table 5 are our specific choices for the exponential inflation constant (ρ), for $g_{preserved_dims}$ and $g_{compressed_dims}$ values, training durations (in Mimgs), and both total and preserved number of dimensions per each schedule and dataset combination. Of note, for the PR-Preserving schedule, we tested two different configurations with smaller and larger noise. These differ by our choice of ρ , with smaller noise using $\rho = 1$ and larger range using $\rho = 2$. Both hyper-parameter choices produce qualitatively good generated samples, but we noticed that choosing $\rho = 2$ yields better FID scores (if sampling from a standard multivariate normal at $t_0 = T$) and requires smaller training times. Results presented in the main text reflect the larger noise option. For completeness, we also showcase FID results for the smaller noise range networks in Table 6.

All networks were trained on the same DDPM++ architecture, as implemented in [28] and using our proposed preconditioning scheme and factors in the standard (e.g., image space) basis. No gradient clipping or mixed-precision training were used, and all networks were trained to perform unconditional generation. We run training in the image space basis (as opposed to in eigenbasis) because this option proved to be more stable in practice for non-toy datasets. Additionally, we estimate the eigendecomposition of the target datasets before training begins using 50K samples for CIFAR-10 and 15K samples for AFHQv2. Based on our experiments, any sample size above total number of dimensions works well for estimating the desired eigenbasis.

Table 4: CIFAR-10 & AFHQv2 Common Training Hyperparameters (Across All Schedules)

Hyperparameter Name	Hyperparameter Value
Channel multiplier	128
Channels per resolution	2-2-2
Dataset x-flips	No
Augment Probability	12%
Dropout Probability	13%
Learning rate	10^{-4}
LR Ramp-Up (Mimg)	10
EMA Half-Life (Mimg)	0.5
Batch-Size	512

Table 5: CIFAR-10 & AFHQv2 Variable Training Parameters (Per Schedule)

Hyperparameter Name	Dataset	PRP	PRR to 2%	PRR to 10%	PRR to 20%
Training Duration (Mimgs)	CIFAR-10	275	300	450	450
Training Duration (Mimgs)	AFHQv2	275	300	350	350
Exponential Inflation Constant (ρ)	Both	2	1	1	1
Total (Nominal) Dimensions	Both	3072	3072	3072	3072
Dimensions Kept	Both	3072	62	307	615
$g_{preserved_dims}$	Both	1	2	2	2
$g_{compressed_dims}$	Both	1	0.98	0.89	0.75

Times utilized to construct conditioning noise inputs to networks ($\mathbf{c}_{noise}(t)$) were uniformly sampled ($t \sim \mathcal{U}(t_{min}, t_{max})$), with $t_{min} = 10^{-7}$ and $t_{max} = 15.01$, across all experiments. For the AFHQv2 dataset, we chose to adopt a 32x32 resolution (instead of 64x64 as in [28]) due to constraints on training time and GPU availability. Therefore, for our experiments, both datasets have a total of 3072 (i.e., 3x32x32) dimensions.

Finally, all training was performed on single GPUs. As in [28], we report training duration in Mimgs and note that time needed to achieve 200 Mimgs is approximately 2 weeks on NVIDIA RTX 3090 or 4090 GPUs using hyperparameters shown in Tables 4, 5. This training time can be substantially reduced (to approximately 2 days for 200Mimgs) if using same multi-GPU training settings as in [28].

Table 6: FID Values for PR-Preserving Networks Trained with $\rho = 1$

Dataset	FID Mean $\pm 2\sigma$
CIFAR-10	23.14 \pm 0.10
AFHQv2	23.15 \pm 0.06

B.5 Details of Roundtrip MSE and FID calculation Experiments

B.5.1 Roundtrip Experiments

For image datasets (CIFAR-10 and AFHQv2), we simulated full round-trips: integrating the pfODEs (6) forward in time to map original images into latent space and then backwards in time to reconstruct original samples. We run these roundtrips for a set of 10K randomly sampled images, three times per each schedule (PRP, PRR to 2, 10, and 20%) and compute pixel mean squared error between original and reconstructed images, averaged across the 10K samples. Values reported in Table 1 represent mean ± 2 standard deviations of pixel MSE between these three different random seeds per each condition. For pfODE integration, we used the discretization schedule and Heun solver detailed above (Appendix B.3.2), with $t_{max} = 15.01$, $\epsilon_s = 10^{-2}$, and $N = 118$ for all conditions.

Table 7: CIFAR-10 & AFHQv2 FID Experiments Latent Space Compressed Dimensions Variance

Schedule	Latent Space Compressed Dimensions Variance
PRR to 2%	2.15×10^{-7}
PRR to 10%	5.6×10^{-8}
PRR to 20%	6.8×10^{-9}

B.5.2 FID Experiments

For image datasets, we also computed Frechet Inception Distance (FID) scores [46] across 3 independent sets of 50K random samples, per each schedule (PRP, PRR to 2, 10, 20%). Values reported in Table 1 represent mean ± 2 standard deviations across these 3 sets of random samples per each condition. Here again, we used the discretization scheme and solver described in Appendix B.3.2 with $t_{max} = 15.01$, $\epsilon_s = 10^{-2}$, and $N = 256$ across all conditions. We chose $N = 256$ here (instead of 118) because this provided some reasonable trade-off between improving FID scores and reducing total compute time.

To obtain our latent space random samples $\mathbf{x}(T)$ at time $t_0 = T$ (i.e., at the start of generation) we sample from a diagonal multivariate normal with either 1) all diagonal elements being 1 (for PR-Preserving schedule) or 2) all elements corresponding to preserved dimensions being 1 and all elements corresponding to compressed dimensions being equal to the same small value for a given PR-Reducing schedule (see Table 7).

B.6 Details of Toy Alpha-Shape/Mesh Coverage Experiments

To assess numerical error incurred when integrating our proposed pfODEs, we performed coverage experiments using 3D meshes and 2D alpha-shapes [72, 73] in select toy datasets (i.e., 2D circles and 3D S-curve). If our numerical integration were perfect, points initially inside these sets should remain inside at the end of integration; failure to do so indicates miscalibration of the set’s coverage. For these experiments, we sampled 20K test points from a Gaussian latent space with appropriate diagonal covariance. For PR-Preserving schedules, this is simply a standard multivariate normal with either 2 or 3 dimensions. For PR-Reducing experiments, this diagonal covariance matrix contains 1’s for dimensions being preserved and a smaller value (10^{-2} for Circles, 2.5×10^{-3} for S-curve) for dimensions being compressed.

Next, we sampled uniformly from the surfaces of balls centered at zero and with linearly spaced Mahalanobis radii ranging from 0.5 to 3.5 (200 pts per ball). We then fit either a 2D alpha-shape (2D Circles) or a mesh (3D S-Curve) to each one of these sets of points. These points thus represent “boundaries” that we use to assess coverage prior to and after integrating our pfODEs. We define the initial coverage of the boundary to be the set of points (out of 20K test points) that lie inside the boundary. We then integrate the pfODE backward in time (the “generation” direction) for each sample and boundary point. At the end of integration, we again calculate the mesh or 2D alpha-shape and assess the number of samples inside, yielding our final coverage numbers.

Similarly, we take our samples and boundary points at the end of generation, simulate our pfODEs forwards (i.e., the “inflation” direction), and once again, use 2D alpha-shapes and meshes to assess coverages at the end of this round-trip procedure. As shown in Figure 4 (panels (B), (C)), we are able to preserve coverage up to some small, controllable amount of error for both schedules and datasets using this process.

When performing PR-Reducing simulations in these experiments, we chose $g_{preserved_dims} = 1.15$ (circles, s curve) and $g_{compressed_dims} = 0.85$ (circles) or $g_{compressed_dims} = 0.70$ (S-curve). This was necessary in practice to avoid numerical underflow errors that arose from fitting 2D alpha-shapes or meshes to highly compressed (approximately low-rank) Gaussian latent spaces.

C Appendix: Additional Experiments and Supplemental Information

C.1 Spectra and PR-Dimensionality for a few common image datasets

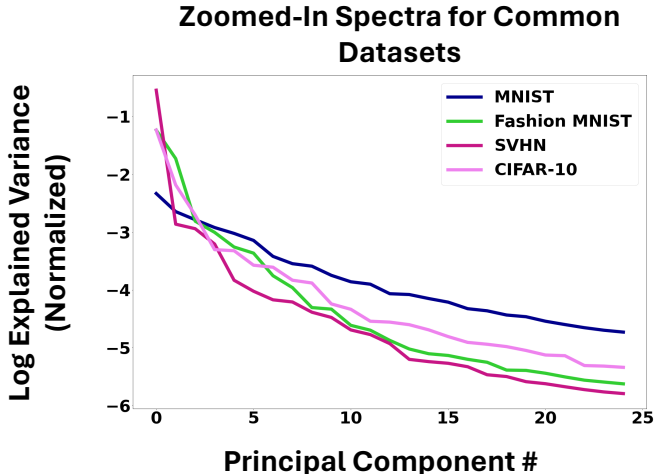


Figure 7: **Zoomed-in spectra for some standard image datasets.** Log of explained variance versus number of principal components (PCs) for 4 common image datasets (MNIST, Fashion MNIST, CIFAR-10, and SVHN). We plot only the first 25 PCs across all datasets to facilitate comparison.

Table 8: Participation ratio (PR) for some commonly used image datasets.

Dataset	PR
MNIST	30.69
Fashion MNIST	7.90
SVHN	2.90
CIFAR-10	9.24

C.2 Additional Toy Experiments

C.2.1 Toy Experiments on Datasets with Lower Intrinsic Dimensionality

The pfODEs proposed here allow one to infer latent representations of data that either preserve or reduce intrinsic dimensionality as measured by the participation ratio. In this context, it is important to characterize our PR-Preserving pfODEs’ behavior in cases where data are embedded in a higher-dimensional space but are truly lower-dimensional (e.g., 2D data embedded in 3D space). In such cases, one would expect inflationary pfODEs to map data into a low-rank Gaussian that preserves the true intrinsic PR-dimensionality of the original data.

To confirm this intuition, we constructed 3D-embedded (2D) circles datasets using two different approaches: (1) by applying an orthonormal matrix M to the original data points, embedding them into 3D as a tilted plane (**Figure 8**, top 2 rows) or (2) constructing a third coordinate using $z = \text{sign}(y)y^2$, which creates a curved (chair-like) shape in 3D (**Figure 8**, bottom 2 rows). We then simulated our PR-Preserving pfODE for both embedding procedures and considering both the case in which no noise was added to the data or, alternatively, where some Gaussian noise is added to the initial distribution, giving it a small thickness. We used zero-mean Gaussian noise with σ of 0.2 and 0.5 for embedding types (1) and (2), respectively.

As shown in **Figure 8**, when no noise is added, our PR-Preserving pfODEs Gaussianize the original data points along the manifold plane (rows 1 and 3, rightmost columns). Alternatively, when noise is added and the manifold plane has some “thickness” the inflationary flows map original data into a lower-rank Gaussian (rows 3 and 4, rightmost columns). In both cases, the original PR is preserved (up to some small numerical error), as expected.

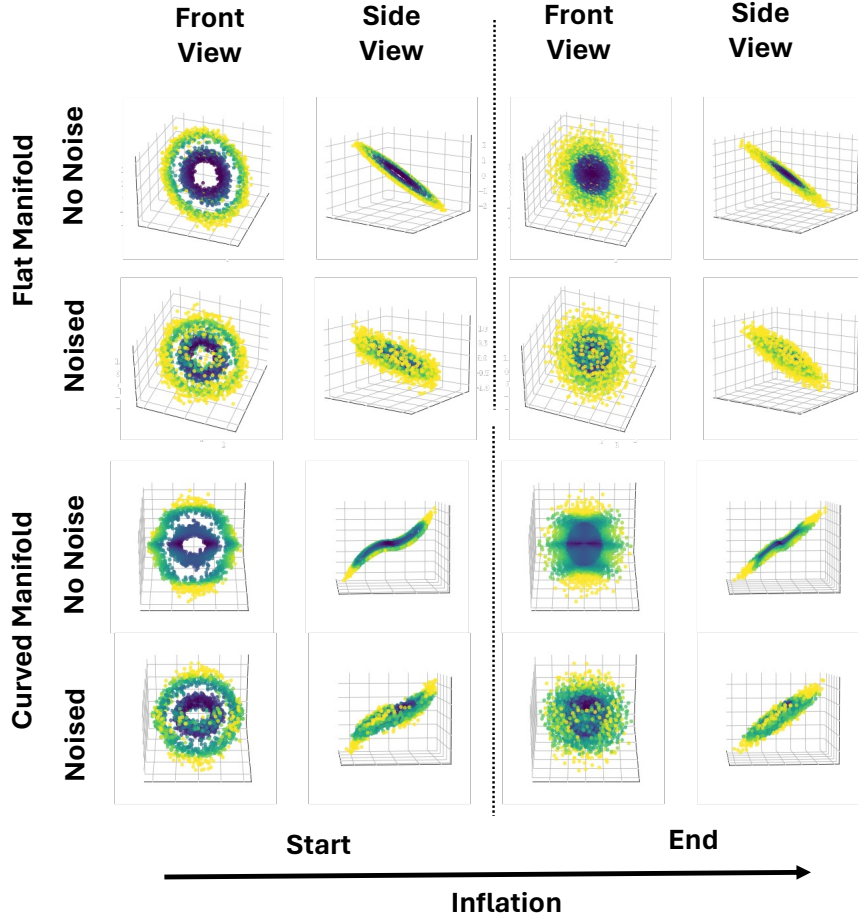


Figure 8: **Additional PR-Preserving experiments for 2D data embedded in 3D space.** Here we integrate our PR-Preserving pODEs forwards in time (i.e., inflation) for 2 different toy datasets, constructed by embedding the 2D Circles data in 3 dimensional space as either a flat (top rows) or a curved (bottom rows) manifold. We present results for such simulations both without any added noise (1st and 3rd rows) and with some small added noise (0.2 and 0.5 σ for flat and curved cases, respectively - 2nd and 4th rows).

C.2.2 3D Toy PR-Reducing Experiments with Different Dimension Scaling

For our 3D toy data PR-Reducing experiments, we tested how changing the relative scaling of different dimensions in the original datasets qualitatively changes generative performance.

For the first experiment, we scaled all dimensions to variance 1 (**Figure 9, first and third rows**). In this case, all dimensions contribute equally to total variance in the data. In contrast, for the second experiment (**Figure 9, second and fourth rows**), we scaled the thickness dimension to variance 0.5 and all others to 1. In this case, the non-thickness dimensions together account for most of the total variance.

We then trained neural networks on 3D S-curve and Swirl data constructed using these two different scaling choices and used these networks to simulate our PR-Reducing pODEs (reduction from $3D \rightarrow 2D$) both forwards (**Figure 9 left panels**) and backwards (**Figure 9 right panels**) in time. Of note, the first scaling choice leads to generated samples that seem to loose some of the original shape content of the target dataset (first and third rows, rightmost columns). In contrast, scaling choice 2 is able to almost perfectly recover the original shapes (second and fourth rows, rightmost columns). This is because scaling the thickness dimension to 0.5 reduces the percent of total variance explained along that axis, and our PR reduction preferentially compresses in that direction, preserving most

Additional Toy $3D \rightarrow 2D$ Dimension-Reducing Simulations

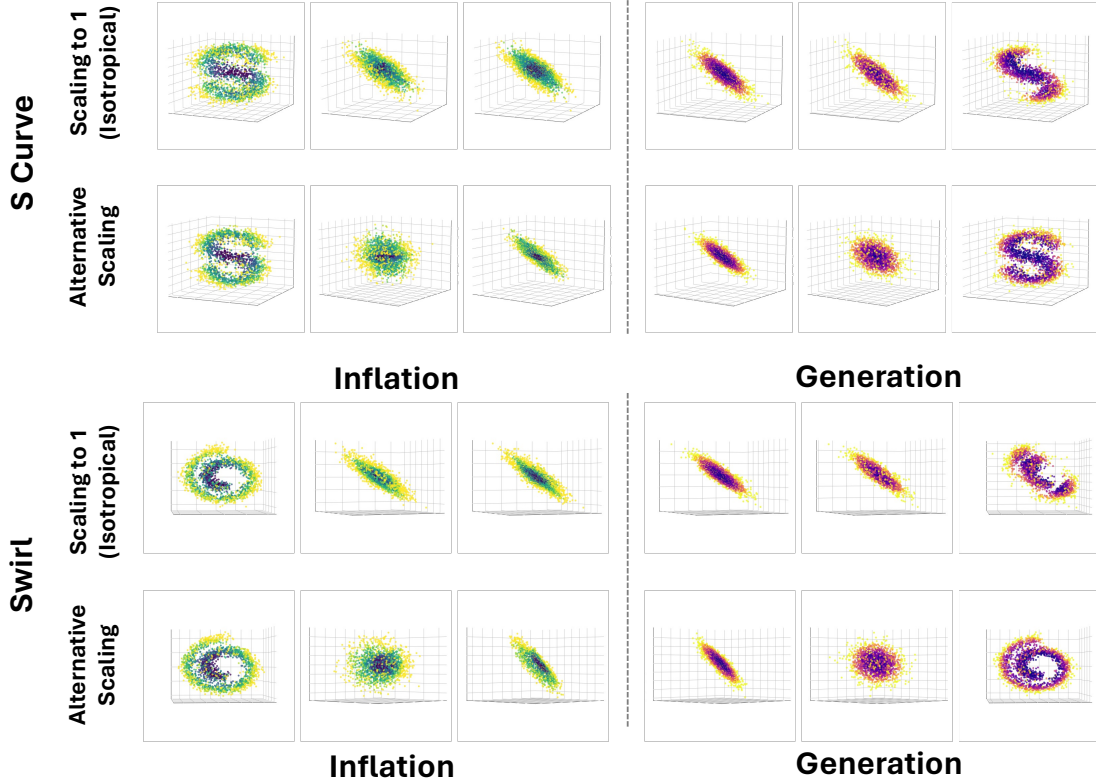


Figure 9: **Toy $3D \rightarrow 2D$ dimension-reducing experiments with alternative scalings.** Shown here are simulations of our $3D \rightarrow 2D$ PR-Reducing pODEs for 3D toy datasets (S-curve, Swirl) scaled either to unit variance across all 3 dimensions (first and third rows) or scaling the thickness dimension to 0.5, while leaving other dimensions scaled to 1 (second and fourth rows). Note that scaling all dimensions to 1 leads to some loss in original shape content when running generation (first and third rows, rightmost column). This is *not* the case when we make total variance contribution of the “thickness” dimension smaller (i.e., under the alternative scaling; second and fourth rows, rightmost column).

information orthogonal to it. By contrast, the first scaling choice spreads variance equally across all dimensions and, therefore, shape and thickness content of target distribution are more evenly mixed among different eigendimensions. As a result, compressing the last dimension in this case inevitably leads to loss of both shape and thickness content, as observed here.

C.3 Autocorrelation of Network Residuals

In Section 5 above, we considered the possibility that numerical errors in approximating the score function might result in errors in pODE integration and thus miscalibration of our proposed inference procedure. There, we argued that if these score estimation errors can be modeled as white noise, integration using sufficiently small integration step sizes will maintain accuracy, as dictated by theorems on numerical integration of SDEs [41]. Here, we investigate the validity of this approximation for our trained score functions.

As detailed in Appendices B.1 and B.3.1, we did not directly estimate scores but trained networks to estimate a denoiser $\hat{\mathbf{y}} = \mathbf{D}_\theta(\mathbf{x}, \mathbf{C}(t))$, where \mathbf{y} are samples from the data and $\mathbf{x} = \mathbf{y} + \mathbf{n}$ are the noised samples with $\mathbf{n} \sim \mathcal{N}(\mathbf{0}, \mathbf{C}(t))$. In this case, one can then compute scores for the noised

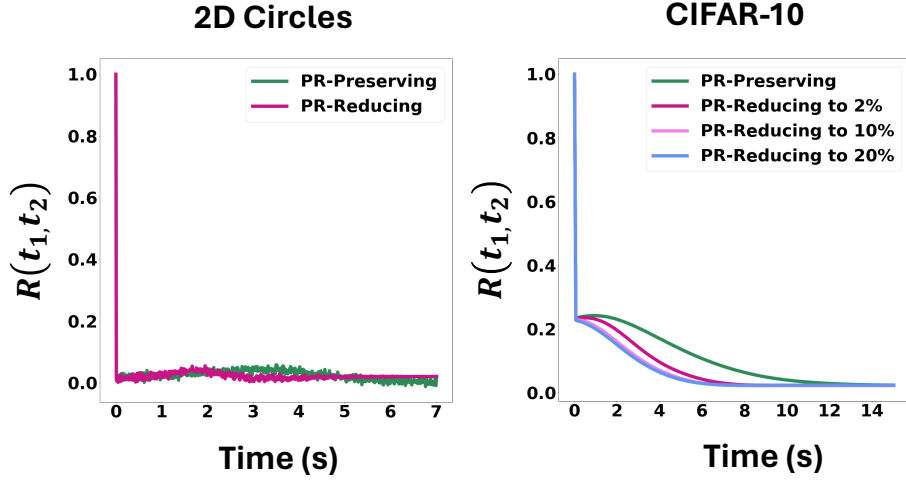


Figure 10: **Autocorrelation of denoiser network residuals.** Scaled autocorrelations of denoising network residuals $\epsilon(\mathbf{x}(t))$ for two sample toy networks (left, 2D circles PR-Preserving (green) and PR-Reducing to 1 dimension (pink)) and for networks trained on CIFAR-10 (right) for both PR-Preserving (green) and all PR-Reducing schedules we trained networks on (i.e., PR-Reducing to 2% (pink), to 10% (violet), and to 20% (blue)). Toy data exhibit minimal autocorrelation along integration trajectories, while the CIFAR score estimates have some autocorrelation along one third to one half of the integration trajectory.

distributions using:

$$\nabla_{\mathbf{x}} \log p(\mathbf{x}, \mathbf{C}(t)) = \mathbf{C}^{-1}(t) \cdot (\mathbf{D}_{\theta}(\mathbf{x}, \mathbf{C}(t)) - \mathbf{x}) \quad (84)$$

In practice, however, this de-noised estimate contains some error $\epsilon = \hat{\mathbf{y}} - \mathbf{y}$, which is the true residual error in our network estimates. Therefore, we rewrite our score expression as:

$$\nabla_{\mathbf{x}} \log p(\mathbf{x}, \mathbf{C}(t)) = \mathbf{C}^{-1}(t) \cdot ((\hat{\mathbf{y}} - \mathbf{x}) + \epsilon) \quad (85)$$

where $(\hat{\mathbf{y}} - \mathbf{x})$ can be understood as the magnitude of the correction made by the denoiser at \mathbf{x} [36]. Note that $\epsilon = \mathbf{0}$ for the ideal denoiser (based on the true score function), but nonzero ϵ will result in errors in our pfODE integration.

As argued above, these errors can be mitigated if they are uncorrelated across the data set, but this need not be true. To assess this in practice, we extracted estimation errors $\epsilon(\mathbf{x})$ across a large number of data samples (10K for 2D circles toys, 50K for CIFAR-10) and for networks trained on both PR-Preserving and PR-Reducing schedules (PR-Reducing to 1D for circles, and to 20%, 10%, and 2% for CIFAR-10) and then computed cross-correlations for these errors along integration trajectories $\mathbf{x}(t)$:

$$\mathbf{R}(t_1, t_2) = \mathbb{E}_{\mathbf{x}}[(\epsilon(\mathbf{x}(t_1)) - \bar{\epsilon})(\epsilon(\mathbf{x}(t_2)) - \bar{\epsilon})^{\top}] \quad (86)$$

where $\bar{\epsilon}$ is the mean residual across the entire data set. In practice, we use scaled correlations in which an entry R_{ij} is normalized by $\sigma_i \sigma_j$ the (zero-lag) variance of the residuals along the corresponding dimensions.

Results of these calculations are plotted in **Figure 10**, for the mean across diagonal elements of \mathbf{R} . As the left panel of **Figure 10** shows, residuals display negligible autocorrelation for networks trained to denoise toy data sets, while for CIFAR-10 (right panel), there is some cross-correlation at small time lags. This is likely due to the increased complexity of the denoising problem posed by a larger data set of natural images, in addition to the limited approximation capacity of the trained network. As a result, points nearby in data space make correlated denoising errors. Nevertheless, this small amount of autocorrelation does not seem to impact the accuracy of our round-trip experiments nor our ability to produce good-quality generated samples (**Figures 5, 6; Table 1**).

C.4 Dataset Pre-Processing

Toy datasets were obtained from `scikit-learn` [74] and were de-meant and standardized to unit variance prior to training models and running simulations. The only exceptions to this are the alternative 3D toy datasets detailed in Appendix C.2.2, where the third dimension was scaled to slightly smaller variance.

For CIFAR-10 and AFHQv2 datasets, we apply the same preprocessing steps and use the same augmentation settings as those proposed for CIFAR-10 in [28] (cf. Appendix F.2), with the only change that we downsample the original AFHQv2 data to 32×32 instead of 64×64 .

C.5 Licenses

Datasets:

- CIFAR-10 [43]: MIT license
- AFHQv2 [44]: Creative Commons BY-NC-SA 4.0 license
- Toys [74]: BSD License